Monthly Notices of the ROYAL ASTRONOMICAL SOCIETY

MNRAS **529,** 587–603 (2024)
Advance Access publication 2024 February 19

https://doi.org/10.1093/mnras/stae517

A hidden population of massive white dwarfs: two spotted K + WD binaries

Dominick M. Rowan [1,2★†] Tharindu Jayasinghe [3†‡] Michael A. Tucker [1,2§] Casey Y. Lam [3] Todd A. Thompson [1,2,4] Christopher S. Kochanek,[1,2] Natasha S. Abrams [3] Benjamin J. Fulton [5] Ilya Ilyin [6] Howard Isaacson [3,7] Jessica R. Lu [3] David V. Martin [1,2] and Belinda Nicholson [7,8]

[1]*Department of Astronomy, The Ohio State University, 140 West 18th Avenue, Columbus, OH 43210, USA*
[2]*Center for Cosmology and Astroparticle Physics, The Ohio State University, 191 W. Woodruff Avenue, Columbus, OH 43210, USA*
[3]*Department of Astronomy, University of California Berkeley, Berkeley CA 94720, USA*
[4]*Department of Physics, The Ohio State University, Columbus, OH 43210, USA*
[5]*NASA Exoplanet Science Institute/Caltech-IPAC, Pasadena, CA 91125, USA*
[6]*Leibniz Institute for Astrophysics Potsdam (AIP), An der Sternwarte 16, D-14482 Potsdam, Germany*
[7]*Centre for Astrophysics, University of Southern Queensland, Toowoomba 4350, Australia*
[8]*Sub-Department of Astrophysics, University of Oxford, Keble Rd, Oxford OX13RH, UK*

Accepted 2024 February 14. Received 2024 February 12; in original form 2023 July 20

ABSTRACT

The identification and characterization of massive ($\gtrsim 0.8\,M_\odot$) white dwarfs is challenging in part due to their low luminosity. Here, we present two candidate single-lined spectroscopic binaries, *Gaia* DR3 4014708864481651840 and 5811237403155163520, with K-dwarf primaries and optically dark companions. Both have orbital periods of $P \sim 0.45$ d and show rotational variability, ellipsoidal modulations, and high-amplitude radial velocity variations. Using light curves from the *Transiting Exoplanet Survey Satellite* (*TESS*), radial velocities from ground-based spectrographs, and spectral energy distributions, we characterize these binaries to describe the nature of the unseen companion. We find that both systems are consistent with a massive white dwarf companion. Unlike simple ellipsoidal variables, star-spots cause the light-curve morphology to change between *TESS* sectors. We attempt to constrain the orbital inclination using PHOEBE binary light-curve models, but degeneracies in the light curves of spotted stars prevent a precise determination. Finally, we search for similar objects using *Gaia* DR3 and *TESS*, and comment on these systems in the context of recently claimed compact object binaries.

Key words: binaries: spectroscopic – white dwarfs.

1 INTRODUCTION

Close binary systems that go through common envelope (CE) evolution can produce a number of unique astrophysical phenomena such as Type Ia supernovae progenitors, cataclysmic variables, and X-ray binaries (e.g. Paczynski 1976; Webbink 1984). Modelling CE evolution is challenging due to the short time-scales and the combination of physical processes involved (e.g. Ivanova et al. 2013; Röpke & De Marco 2023). Standard prescriptions such as the energy formalism, which parametrizes how the dissipated orbital energy is used to eject the envelope (Webbink 1984), are used for individual binaries (e.g. Afşar & Ibanoğlu 2008), simulations (e.g. Sandquist et al. 1998), and in binary population synthesis (e.g. Politano et al. 2010). However, these model parameters are expected to be time-dependent and vary with stellar properties, which makes producing a predictive model using this formalism challenging (De Marco et al. 2011; Röpke & De Marco 2023). By observing the products of CE evolution, we can improve our understanding of binary evolution pathways and the mass distribution of stellar remnants.

In recent years, there has been great interest in searching for non-interacting binaries that contain a compact object (e.g. Breivik, Chatterjee & Larson 2017). While these searches typically focus on identifying black hole binaries (Chakrabarti et al. 2023; El-Badry et al. 2023; Tanikawa et al. 2023), the same astrometric (e.g. Andrews, Breivik & Chatterjee 2019), spectroscopic (e.g. Jayasinghe et al. 2023), and photometric tools (e.g. Rowan et al. 2021; Green et al. 2023) have been applied to identify neutron star candidates (Lin et al. 2023; Zheng et al. 2023).

Many of the false positives in the search for non-interacting black hole binaries are actually luminous binaries, often with deceptive mass transfer histories (e.g. El-Badry et al. 2022; Jayasinghe et al. 2022). Massive white dwarfs (WDs) can also be detected as 'false positives' in these surveys, and measuring WD mass distributions is relevant to understanding the pulsating phases of the asymptotic giant

★ E-mail: rowan.90@osu.edu
† These authors contributed equally to this work.
‡ NASA Hubble Fellow.
§ CCAPP Fellow

branch as well as the chemical evolution of galaxies (Catalán et al. 2008; Cummings et al. 2018). The WD mass distribution is generally understood to peak at $M \sim 0.6\,M_\odot$ with an additional peak near $M \sim 0.8\,M_\odot$ (Camisassa et al. 2019). Detecting and characterizing WDs in the high-mass tail of this distribution is important for understanding the properties of these dense stellar remnants and the progenitors of Type Ia supernovae. Outside of binary systems, detecting isolated massive WDs is challenging since more massive WDs are more compact and therefore are less luminous. However, by observing the radial velocity (RV) and photometric variability of luminous companions, we should be able to find many examples of non-interacting massive WDs.

The majority of WD binaries in main-sequence binaries have M-dwarf companions (Rebassa-Mansergas et al. 2010). Since CE evolution is expected to be dependent on the mass of both stars, there have been efforts to identify WD + FGK binaries using broad-band photometry and ultraviolet (UV) spectroscopy (Parsons et al. 2015; Hernandez et al. 2021, 2022a), but few massive WDs have been identified through this approach (e.g. Wonnacott, Kellett & Stickland 1993; Hernandez et al. 2022b).

Here, we present two candidate post-CE WDs with K-dwarf companions identified through RV observations. In Section 2, we describe how these systems were identified and the follow up RV observations. In Section 3, we combine the RVs with broad-band photometry to characterize the binaries and their photometric variability. The late-type main-sequence stars are chromospherically active in both binaries, producing star-spots that modify the observed ellipsoidal variability. In Section 4, we show the limitations that star-spots place on our ability to constrain the WD mass. Finally, in Section 5, we describe these systems in context with other WD and neutron star binaries detected in RV surveys.

2 TARGET IDENTIFICATION AND OBSERVATIONS

We identified high-amplitude RV and photometric variability in two K-dwarfs, LAMOST J120802.64 + 311103.9 (hereafter J1208, Cui et al. 2012) and *Gaia* DR3 5811237403155163520 (hereafter J1721, Gaia Collaboration 2016, 2023). Both systems show short-period photometric variability in *Transiting Exoplanet Survey Satellite* (*TESS*, Ricker et al. 2015) consistent with ellipsoidal variability. For both systems, we obtain follow-up RV observations to fully characterize the binary orbits. Table 1 reports summary parameters of these two targets. In Sections 2.1 and 2.2, we describe how we identified these targets and the spectroscopic and photometric observations used to characterize them.

2.1 J1208

J1208 (*Gaia* DR3 4014708864481651840) was originally identified as a non-interacting compact object binary candidate by Mu et al. (2022) using multi-epoch spectra from the Large Sky Area Multi-Object Fiber Spectroscopy Telescope (LAMOST, Cui et al. 2012). There are three low-resolution LAMOST spectra of J1208, taken on 2013 May 10, 2015 March 12, and 2016 December 16. Mu et al. (2022) report an RV amplitude $\Delta V_R = 262\,\mathrm{km\,s^{-1}}$ and a spectral type of K-dwarf plus dwarf carbon star (K3 + dCK, Roulston, Green & Kesseli 2020). They identify photometric variability with a period of $P = 0.4630$ d and find a binary mass function $f(M) = 0.11\,M_\odot$. *Gaia* also reports a large RV amplitude $A_{\rm RV} = 366\,\mathrm{km\,s^{-1}}$ for this target. This value is computed as the difference between the largest and smallest RVs measured after outlier removal.

Table 1. Summary information for J1208 and J1721. The orbital periods are determined from the *TESS* light curves (Section 3.1) and the velocity semi-amplitudes are measured from the spectroscopic orbits (Section 3.2). Extinctions are estimated using `mwdust` (Bovy et al. 2016). $N_{\rm TESS}$ and $N_{\rm RV}$ report the number of *TESS* sectors and the number of RV observations, respectively. We use SEDs to estimate the photometric primary mass and radius (Section 3.4).

	J1208	J1721
RA (°)	182.01141	260.46121
Dec. (°)	31.18433	−68.74177
GDR3 source	4014708864481651840	5811237403155163520
Distance (pc)	$88.6^{+0.1}_{-0.2}$	$250.5^{+0.6}_{-0.8}$
$A_{\rm RV}$ ($\mathrm{km\,s^{-1}}$)	366	959
Gaia G (mag)	11.42	12.68
A_V (mag)	0.00	$0.1071^{+0.0003\ddagger}_{-0.0003}$
$N_{\rm TESS}$	2	3
$N_{\rm RV}$	12†	5
Period (d)	0.46319 ± 0.00004	0.44690 ± 0.00003
K ($\mathrm{km\,s^{-1}}$)	161 ± 2	186 ± 3
$f(M)$ ($M_\odot$)	0.201 ± 0.008	0.30 ± 0.02
M_1 ($M_\odot$)	0.76 ± 0.02	0.86 ± 0.01
R_1 ($R_\odot$)	0.73 ± 0.02	0.877 ± 0.008
UV excess	✓	✓
X-ray detection	✓	✗

Notes.† We exclude the three LAMOST observations from the RV orbit fits since they occur $\gtrsim 4400$ cycles before the PEPSI/APF observations.
‡ The uncertainty on the extinction is estimated by sampling over the *Gaia* distance posteriors, but we note that this is likely an underestimate since it does not incorporate any intrinsic uncertainties in the `mwdust` dust maps.

We obtained three additional high-resolution ($R \approx 43\,000$) spectra on 2023 February 9 using the Potsdam Echelle Polarimetric and Spectroscopic Instrument (PEPSI, Strassmeier et al. 2015) on the *Large Binocular Telescope*. Each observation had a 10 min integration time with the 300 μm fibre and two cross-dispersers covering 4758–5416 and 6244–7427 Å. We also obtained six observations with the Automated Planet Finder (APF) Levy spectrograph at the Lick Observatory ($R \approx 80\,000$, Vogt et al. 2014) on 2023 February 9, 13, and 17, 2023 May 20 and 21, and 2023 June 16. The first observation had an integration time of 10 min and the others had an integration time of 15 min. The observations used the 2 arcsec × 3 arcsec Decker-T slit. The APF spectra have a wavelength range of 3730–10206 Å and the raw 2D echelle spectra are reduced to 1D spectra through the California Planet Survey (Howard et al. 2010) pipeline. Next, the 1D echelle spectra are continuum normalized and the orders are combined. APF and PEPSI RVs were derived by cross-correlating the continuum normalized spectrum with synthetic spectra using iSpec (Blanco-Cuaresma et al. 2014; Blanco-Cuaresma 2019) with the templates broadened to match the resolution of the data. Table 2 reports the RV observations of J1208.

J1208 was observed by the *TESS* in sectors 22 (2020 March) and 49 (2022 March). We downloaded light curves from the Quick-Look Pipeline (QLP, Huang et al. 2020a, b). We use the raw, undetrended light curves rather than the detrended light curves since the detrending procedure can often remove variability on time-scales >0.3 d (Green et al. 2023). Each sector shows clear periodic variability, as shown in the top panel of Fig. 1. We also retrieve archival photometry from the All-Sky Automated Survey (ASAS, Pojmanski 1997), the All-Sky Automated Survey for Supernovae (ASAS-SN, Shappee et al. 2014; Kochanek et al. 2017; Hart et al. 2023) and the *Wide-field Infrared Survey Explorer* (*WISE*, Wright et al. 2010).

Table 2. RV observations for J1208. We do not use the LAMOST observations for fitting the RV orbit (Section 3.2) because of the large gap between the LAMOST and PEPSI/APF observations.

JD	RV ($km\,s^{-1}$)	σ_{RV} ($km\,s^{-1}$)	Instrument
2456423.04236	43.46	5.36	LAMOST-LRS
2457094.18750	− 166.40	4.49	LAMOST-LRS
2457739.42917	− 128.55	6.33	LAMOST-LRS
2459984.86601	− 127.30	4.40	PEPSI
2459984.94437	− 171.60	4.40	PEPSI
2459985.03646	− 25.40	4.50	PEPSI
2459989.01660	− 100.67	3.78	APF
2459984.96948	− 140.56	3.65	APF
2459992.94531	60.92	3.89	APF
2460084.75719	153.85	3.78	APF
2460085.83655	− 97.89	3.84	APF
2460111.81262	− 152.04	4.00	APF

2.2 J1721

We identified J1721 as a *Gaia* photometric variable with a high RV amplitude. *Gaia* characterized this source a short time-scale photometric variable with $P = 0.22347$ d (Eyer et al. 2023). *Gaia* also reports an `rv_amplitude_robust` of $A_{RV} = 959.2\ km\,s^{-1}$. For comparison, J1208 has $A_{RV} = 366.3\ km\,s^{-1}$, and only 1278 stars in *Gaia* DR3 have $A_{RV} > 500.0\ km\,s^{-1}$. Fig. 2 shows these 1278 stars on a *Gaia* colour–magnitude diagram (CMD) and highlights J1208 and J1721. The majority of high A_{RV} targets sit on the upper main sequence. The narrow wavelength range of the *Gaia* Radial Velocity Spectrometer (846–870 nm, Cropper et al. 2018) was designed to measure RVs of cool stars, and RVs for hot stars ($6900 < T_{eff} < 14500$ K) only became available with *Gaia* DR3 (Blomme et al. 2023). It seems likely that many of the high A_{RV} stars on the upper main sequence suffer from systematic effects. Below $M_G \lesssim 3.5$ mag, almost all of the high A_{RV} targets appear consistent with the binary star main sequence. We selected J1721 for additional follow-up because of its CMD position near a single star isochrone, its periodic photometric variability, and its high RV amplitude.

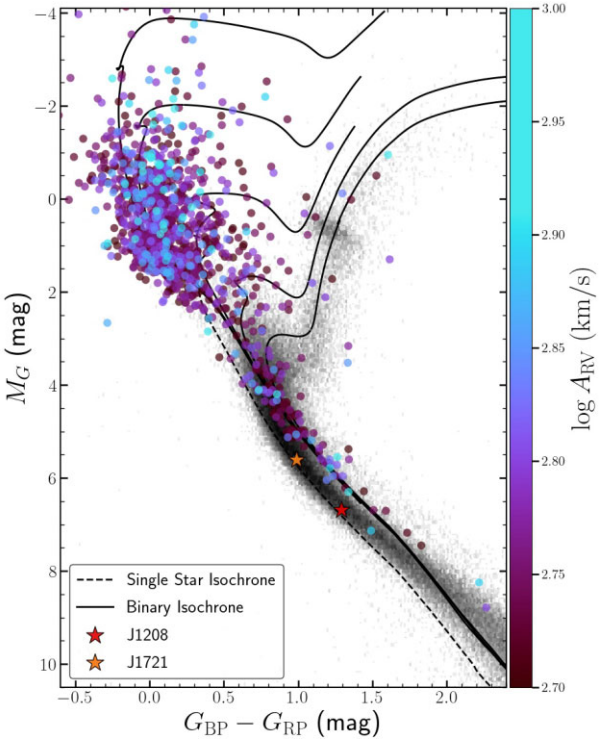

Figure 2. *Gaia* DR3 CMD of a sample of random *Gaia* targets (gray background) and $A_{RV} > 500\ km\,s^{-1}$ targets (coloured). The solid black lines show MIST isochrones (Choi et al. 2016; Dotter 2016) corresponding to an equal mass binary and the dashed line shows a single-star isochrone. Extinctions are determined using `mwdust` with distances from Bailer-Jones et al. (2021). J1208 and J1721 are shown as the red and orange points.

We obtained multi-epoch spectra with CHIRON (Tokovinin et al. 2013) on the Small and Moderate Aperture Research Telescope System (SMARTS) 1.5-m telescope (Schwab et al. 2012) to validate

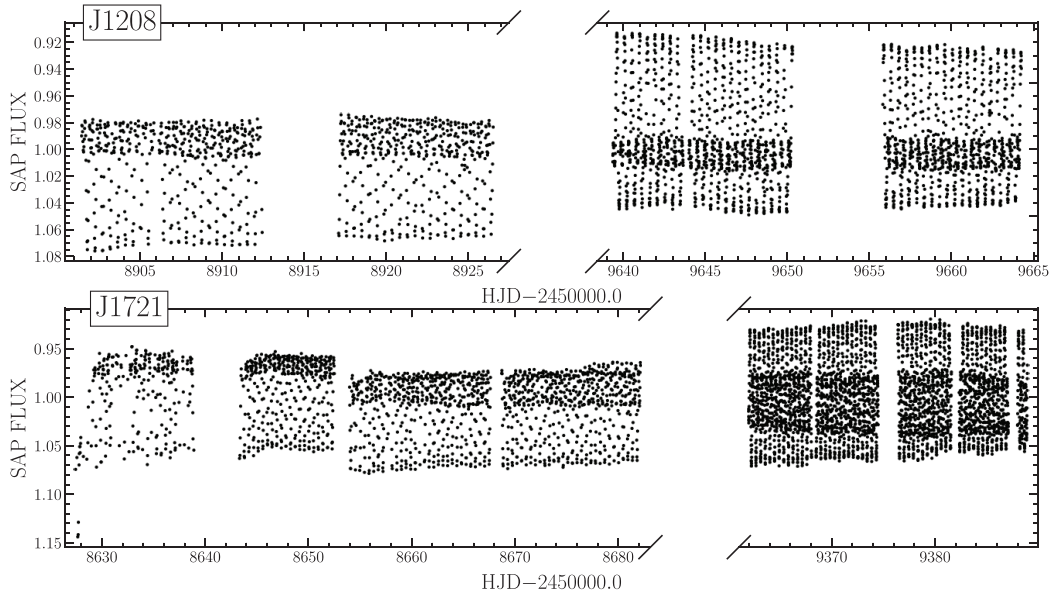

Figure 1. *TESS* light curves of J1208 (top) and J1721 (bottom). Both targets show clear periodic variability as well as long-term modulations between *TESS* sectors.

Table 3. CHIRON RV observations for J1721.

JD	RV (km s^{-1})	σ_{RV} (km s^{-1})	Instrument
2460004.85545	− 92.871	2.433	CHIRON
2460006.89372	− 60.458	1.013	CHIRON
2460007.88454	− 221.646	8.559	CHIRON
2460008.85706	− 142.257	3.132	CHIRON
2460010.88317	23.665	1.379	CHIRON

the orbit and determine the nature of the companion. We obtained five spectra, each with the fibre mode, which uses 4 × 4 pixel binning ($R \approx 28\,000$), and a Th-Ar comparison lamp. Four observations had 20 min integration times, and one had a 30 min integration time. RVs were derived using a least-squares deconvolution against a non-rotating synthetic spectral template, as in Zhou et al. (2020). Table 3 reports the RV observations of J1721.

J1721 was observed by *TESS* in sectors 12 (2019 June), 13 (2019 July) and 39 (2021 June). The bottom panel of Fig. 1 shows the variability, which is clearly periodic but changes between *TESS* sectors. As with J1208, we also retrieve archival photometry from ASAS-SN, *WISE*, and *Gaia*.

3 BINARY CHARACTERIZATION

3.1 Photometric variability

The *TESS* light curves shown in Fig. 1 reveal periodic variability in both targets. Since the light-curve shape varies between *TESS* sectors, we ran a Lomb–Scargle periodogram (Lomb 1976; Scargle 1982) on each sector independently. To estimate the uncertainty in the period, we performed 10^4 bootstrap iterations for each *TESS* sector. Fig. 3 shows the phase-folded light curves for each *TESS* sector.

The *TESS* light curves show ellipsoidal modulations caused by the tidal distortion of the K-dwarf by a close stellar companion. Ellipsoidal variable (ELLs) light curves are typically double-peaked with uneven minima. Both J1208 and J1721 also have uneven maxima in their light curves. While some asymmetry in the maxima is expected in short-period binaries due to relativistic beaming (Loeb & Gaudi 2003; Masuda & Hotokezaka 2019), the large difference between the light-curve maxima and the variations between *TESS* sectors instead suggests that the K-dwarfs are heavily spotted. Since spots evolve over time-scales of tens to hundreds of days (e.g. Giles, Collier Cameron & Haywood 2017), the light-curve shape changes dramatically between *TESS* sectors.

We compute the orbital period independently for each *TESS* sector. The period varies by ∼15–20 min, but this is not a statistically significant difference. Small variations between the periods of each sector could be evidence of latitudinal differential rotation or slightly asynchronous rotational and orbital periods. Taking the median period from the different sectors, we find $P = 0.46319 \pm 0.00004$ and 0.44690 ± 0.00003 for J1208 and J1721, respectively. The period for J1721 is approximately twice the value reported in *Gaia* DR3 (Eyer et al. 2023) as expected for ellipsoidal variability.

The archival ASAS and ASAS-SN light curves of J1208 shown in Fig. 4 suggest long-term variations that could be evidence of spot modulations or star cycles. Both light curves show periodic variability at ∼0.46 d corresponding to the orbital period identified in the *TESS* light curve. In the combined ASAS + ASAS-SN *V*-

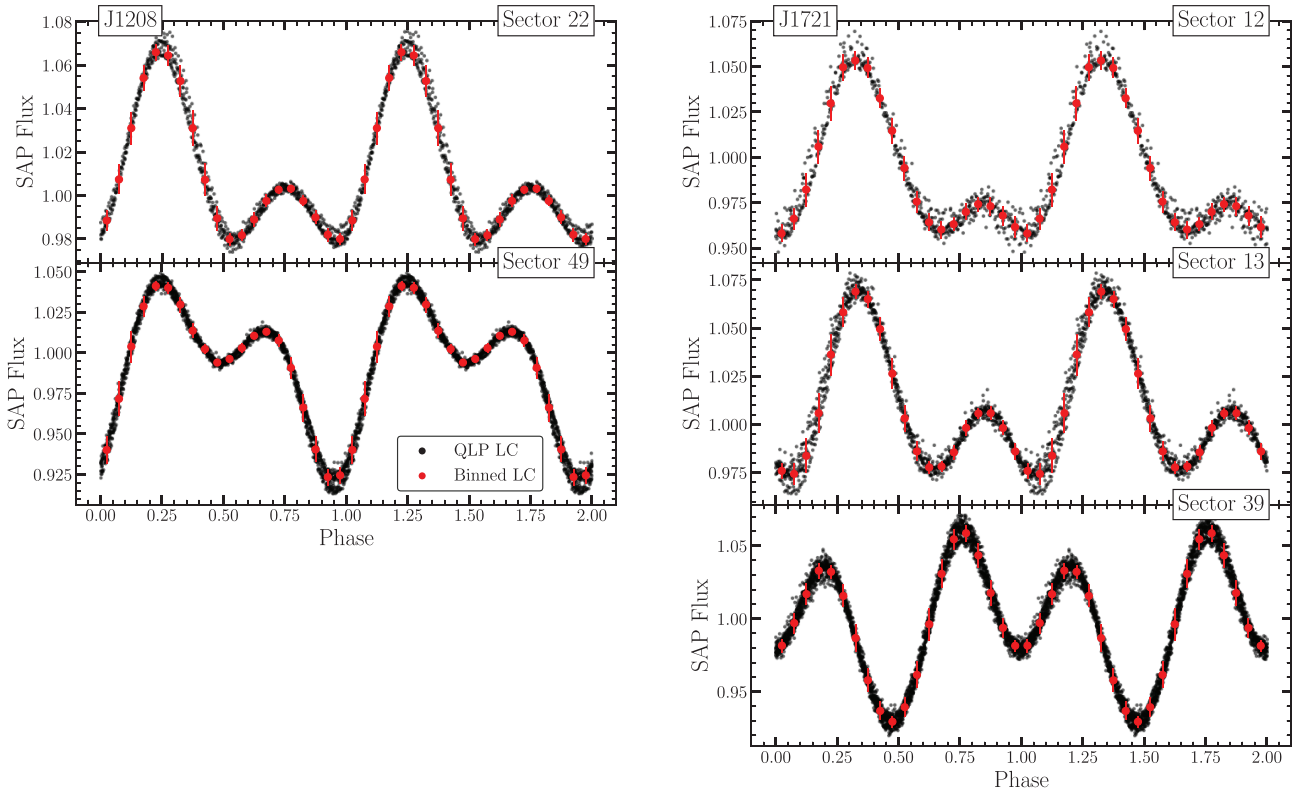

Figure 3. Phase-folded *TESS* light curves of J1208 (left) and J1721 (right). Both systems show short-period ellipsoidal modulations with asymmetric maxima. The light-curve shape varies dramatically between *TESS* sectors, suggesting the presence of spots that evolve on short time-scales. Orbital phase is defined such that RV maxima occurs at phase $\phi = 0.75$.

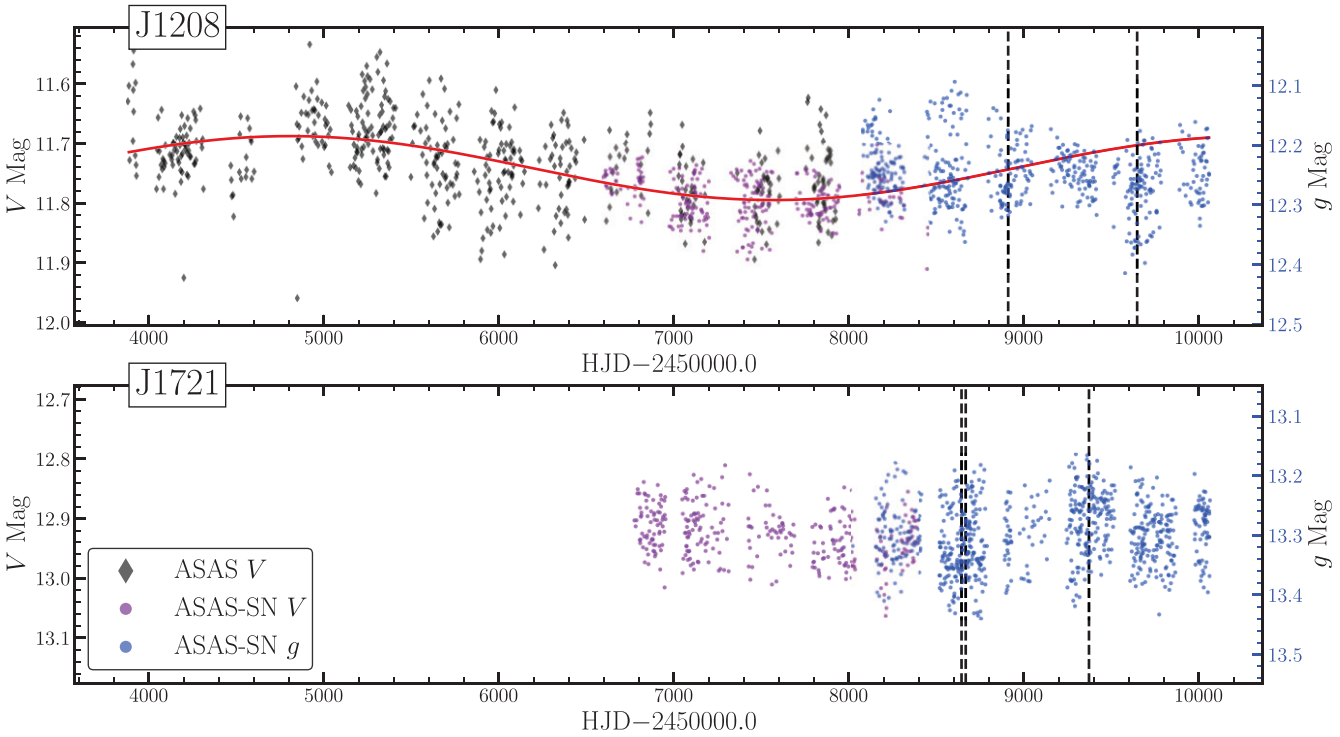

Figure 4. ASAS and ASAS-SN light curves of J1208 (top) and (J1721) bottom. We find some evidence of long-term variability at ∼5520 d in the J1208 light curve, indicated by the red curve. The vertical dashed lines indicate the median times of the *TESS* sectors shown in Fig. 3.

band light curve, we also find evidence for periodic variability at ∼5520 d (∼15.1 years), which could be representative of a stellar activity cycle. The ASAS-SN *g*-band data do not appear to follow this trend, and a Lomb–Scargle periodogram of the combined *V*- and *g*-band light curve, with an offset applied to the *g*-band data to align it with the *V*-band data, did not yield significant periods other than the ∼0.46 d signal. There do appear to be long-term variations in the *g*-band data, which is slightly bluer than the *V* band and includes the calcium H and K lines with rest wavelengths 3969 and 3934 Å, respectively. The *V*- and *g*-band light curves may therefore trace different time-scales of stellar activity (e.g. Mignon et al. 2023).

The ASAS-SN light curve of J1721 does not show similar long-term variations despite the clear sector-to-sector variations in the *TESS* light curve. This could suggest relatively less chromospheric activity, which is consistent with the lack of Hα emission discussed below (Section 3.3).

We also inspected the phase-folded light curves from ASAS, ASAS-SN, ATLAS, *Gaia*, and *WISE* for both systems when available. Unsurprisingly, the multiyear light curves folded at the periods from the *TESS* observations have substantial scatter due to spot evolution.

3.2 Spectroscopic orbits

Since both targets are consistent with short-period binaries, we fit a circular Keplarian orbit model of the form

$$\mathrm{RV}(t) = \gamma + K \cos\left(\frac{2\pi}{P}(t - t_0)\right), \quad (1)$$

where K is the velocity semi-amplitude, P is the orbital period fixed at the values from the *TESS* light curves, t_0 is the time of pericentre passage, and γ is the centre-of-mass velocity. Since the archival LAMOST observations of J1208 were taken $\gtrsim$ 4400 cycles before the PEPSI/APF observations, we chose not to include them in the RV fits since small uncertainties in the orbital period result in large uncertainties in their orbital phase. For J1208, we also fit for an RV offset between the APF and PEPSI measurements. We use the Monte Carlo sampler EMCEE (Foreman-Mackey et al. 2013) to derive the posteriors on K reported in Table 1. For both systems, we find that $K < 0.5A_{\mathrm{RV}}$, indicating that the *Gaia* A_{RV} is overestimated. For J1208, $K = 161 \pm 2\,\mathrm{km\,s^{-1}}$ is consistent with the $\Delta V_R = 262\,\mathrm{km\,s^{-1}}$ reported by (Mu et al. 2022) for the three LAMOST observations (Mu et al. 2022). Fig. 5 shows the RV curves where orbital phase is defined such that RV maxima occurs at phase $\phi = 0.75$.

Even though we expect both short-period binaries to be tidally circularized, we also tested models with non-zero eccentricity. The posteriors on the eccentricity for both targets are peaked at zero eccentricity, with an 84th percentile of $e \leq 0.04$ and ≤ 0.03 for J1208 and J1721, respectively.

The binary mass function relates the velocity semi-amplitude, K, and the orbital period, P, to the masses of the binary components. Throughout this paper, we refer to the photometric primary as M_1 and the unseen companion as M_2. The binary mass function for a circular orbit is

$$f(M) = \frac{PK^3}{2\pi G} = \frac{M_2^3 \sin^3 i}{(M_1 + M_2)^2}. \quad (2)$$

The mass function is the absolute lower limit on the companion mass (M_2) obtained in the limit of an edge-on inclination and a zero mass ($M_1 = 0\,\mathrm{M}_\odot$) photometric primary. Additional constraints on the primary mass, M_1, and the orbital inclination are needed to determine the actual companion mass.

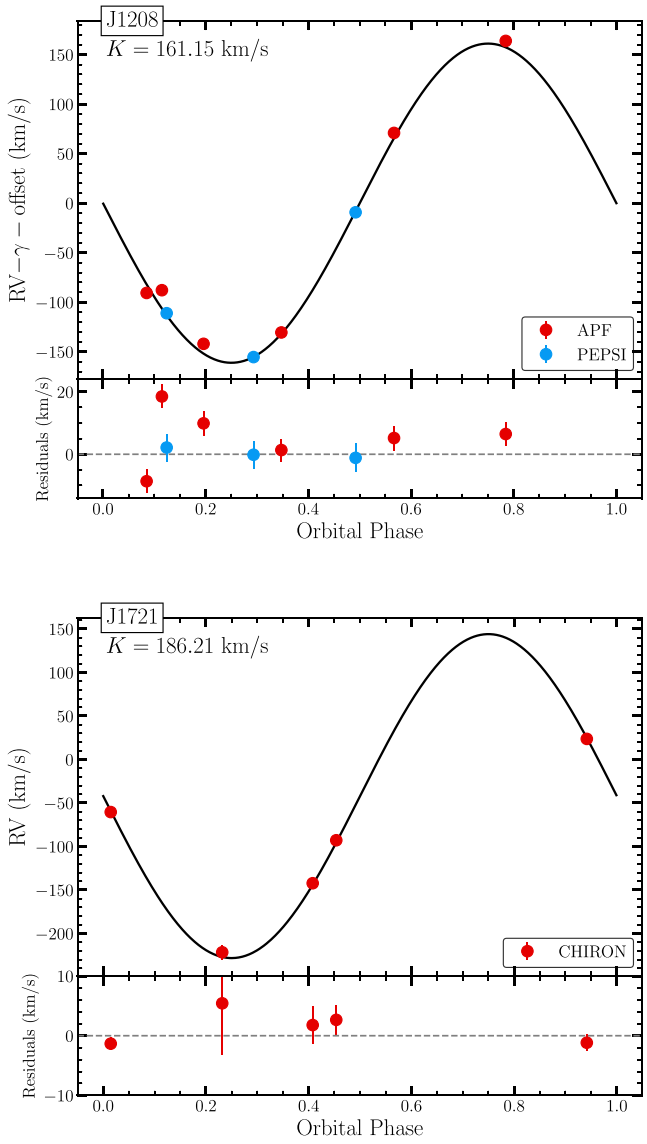

Figure 5. Spectroscopic orbits of J1208 (top) and J1721 (bottom) with residuals. We fit a circular orbit (equation 1) fixed to the photometric period to derive the RV semi-amplitude, K. For J1208, the RVs are shown with the centre-of-mass velocity and the PEPSI RV offset subtracted.

3.3 Hα emission

The APF and PEPSI observations of J1028 show variable Hα emission (Fig. 6). Orbital phase is defined such that the maximum RV occurs at $\phi = 0.75$ and the K star is behind the WD (inferior conjunction) at $\phi = 0$. Three observations with orbital phase $0 < \phi < 0.2$ show strong Hα emission centred on the velocity of the star. One of the two observations between $0.3 < \phi < 0.4$ shows Hα absorption. At $\phi \sim 0.5$, the PEPSI spectra shows double-peaked Hα emission. Hα emission occurs again at $\phi \sim 0.8$.

Hα emission could originate from a combination of chromospheric activity and/or mass transfer. For example, double-peaked emission is commonly seen in accreting compact object binaries (e.g. Swihart et al. 2022). The spectrum with double-peaked emission occurs near phase 0.5 in J1208, when the K-dwarf is in front of the WD. The Hα emission appears to track the motion of the K-dwarf primary, which is also consistent with chromospheric emission seen in similar binaries with compact companions (e.g. Lin et al. 2023; Zheng et al. 2023).

All the CHIRON spectra of J1721 show Hα in absorption (Fig. 6). The lack of Hα emission in J1721 could imply a lower degree of chromospheric activity than in J1208.

The equivalent width of the line changes with orbital phase, with shallower features during phases where the K-dwarf passes in front of the WD. This could suggest that emission from chromospheric activity is filling in the absorption line at these phases. The absorption line is symmetric with respect to the velocity of the K-dwarf, unlike some stripped mass-transfer binaries (e.g. 2MASS J04123153 + 6738486, El-Badry et al. 2022; Jayasinghe et al. 2022). High-resolution infrared spectra of the calcium II triplet (8498, 8542, and 8662Å) could be used to compare the activity indices of these two targets (Martin et al. 2017). The *Gaia* RVS spectrometer does cover this wavelength range, but neither target has an RVS spectrum included in *Gaia* DR3.

3.4 Spectral energy distributions

To determine the properties of the K-dwarfs, we start by using broad-band photometry and single-star evolutionary models. We retrieve Two Micron All Sky Survey (2MASS, Cutri et al. 2003), Wide-Field Infrared Survey Explorer (*WISE*, Cutri & et al. 2012), and Galaxy Evolution Explorer (*GALEX*, Bianchi, Shiao & Thilker 2017) photometry for both targets. We also download the low-resolution *Gaia* XP spectra (De Angeli et al. 2023), which were only available for J1721. For J1208, we use the *Gaia* G, $G_{\rm BP}$, and $G_{\rm RP}$ magnitudes. We fit the spectral energy distributions (SEDs) using the Castelli & Kurucz (2003) atmosphere models included in `pystellibs`.[1] We use `pyphot`[2] to calculate synthetic photometry and sample over stellar parameters with EMCEE (Foreman-Mackey et al. 2013). We keep the distance fixed at the values from Bailer-Jones et al. (2021) and use V-band extinctions from the `mwdust` (Bovy et al. 2016) 'Combined19' dust map (Drimmel, Cabrera-Lavers & López-Corredoira 2003; Marshall et al. 2006; Green et al. 2019). J1208 is within 100 pc and has a high Galactic latitude ($b = 79.7°$) and the 3D dust maps predict zero extinction for this source (Table 1). We do not include the *GALEX* photometry in our SED fits since the spotted primaries are expected to have additional UV flux from chromospheric activity that is not represented in the atmosphere models. WD companions could also contribute to the UV flux.

Fig. 7 shows the SEDs and the fits. We find that J1208 is consistent with a K-dwarf of radius $R_1 = 0.73 \pm 0.02\,{\rm R}_\odot$ and temperature $T_{\rm eff} = 4700 \pm 100$ K and J1721 has radius $R_1 = 0.877 \pm 0.008\,{\rm R}_\odot$ and temperature $T_{\rm eff} = 5100 \pm 20$ K. We also attempt two-star SED fits and find no acceptable solutions with near equal-mass binaries. While the SED does permit having a low-mass companion ($M_2 \lesssim 0.5\,{\rm M}_\odot$), these masses are too small to reproduce the observed RV semi-amplitude even at edge-on inclinations.

The SEDs of both targets have *GALEX* near-ultraviolet (NUV) magnitudes largely consistent with the K-dwarf model. There is an excess far-ultraviolet (FUV) flux of $>5\sigma$ for both J1208 and J1721. The UV excess could be due to chromospheric activity, but, depending on the age of the system, a cool or massive WD could also conceivably produce the observed FUV flux with negligible contributions in the NUV.

[1] https://github.com/mfouesneau/pystellibs
[2] https://mfouesneau.github.io/pyphot/

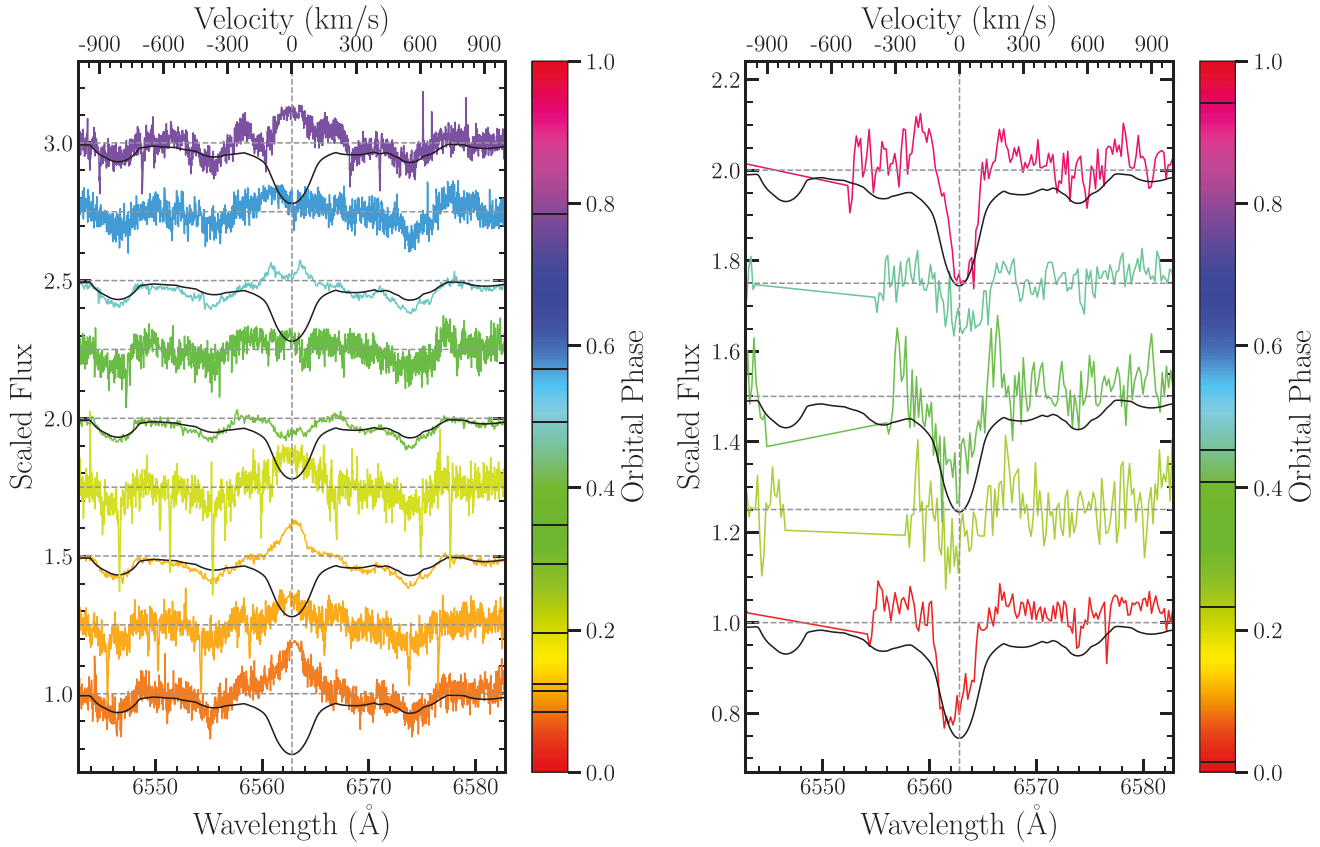

Figure 6. Left: the phase-dependent Hα emission from J1208 in the APF and PEPSI spectra. The spectra have been shifted to the rest frame of the K-dwarf. For comparison, in black we show the absorption line from a synthetic spectrum computed using the stellar effective temperature, surface gravity, metallicity, and rotational broadening. Right: the phase-dependent Hα absorption feature of J1721 from the CHIRON spectra. Unlike J1208, this binary does not show strong emission features. For comparison, the black lines in both panels show the absorption line from a synthetic spectrum computed using the stellar effective temperature, surface gravity, metallicity, and rotational broadening for each target.

J1208 was detected as an X-ray source in *ROSAT* (Voges et al. 1999) with a separation of <15 arcsec. Kiraga & Stępień (2013) report an X-ray to bolometric flux ratio $\log(F_x/F_b) = -3.25 \pm 0.25$ for J1208. Pizzolato et al. (2003) measured the relationship between *ROSAT* X-ray flux and rotation period for different mass bins using *Kepler* rotational variables. For stars $0.63 < M/\mathrm{M}_\odot < 0.78$, they find that the X-ray to bolometric luminosity ratio saturates at $\log(L_x/L_b) = -3.1 \pm 0.2$ below rotation periods of 3.3 ± 1.5 d. Since this is consistent with the X-ray luminosity of J1208, the system's X-ray emission could come entirely from chromospheric activity. *SWIFT* UV photometry or *Hubble Space Telescope* (*HST*) UV spectroscopy could provide meaningful constraints on the nature of this high-energy emission. J1721 has no reported X-ray detection.

We combine the SED radius and temperature measurements with evolutionary tracks from MESA Isochrones and Stellar Tracks (MIST, Choi et al. 2016; Dotter 2016) to estimate the mass of the photometric primary. We use Solar metallicity MIST evolutionary tracks covering the mass range 0.5–1.0 $\mathrm{M}_\odot$. We construct linear interpolations of the stellar radius and effective temperature with age for a grid of masses. We use EMCEE (Foreman-Mackey et al. 2013) to sample over stellar mass and age. We run Markov chain Monte Carlo (MCMC) for 1000 iterations and use a burn-in of 5000 iterations and find $M_1 = 0.76 \pm 0.02\,\mathrm{M}_\odot$ for J1208 and $M_1 = 0.86 \pm 0.01\,\mathrm{M}_\odot$ for J1721. This mass estimate assumes a Solar metallicity and the underlying SED constraints use a fixed distance and extinction. We also fit for the mass using a lower metallicity [Fe/H] $= -0.5$ evolutionary tracks, but find worse agreement with the effective temperature and radius. Both of these binaries almost certainly went through at least one episode of CE evolution, introducing additional uncertainty in the primary mass.

Fig. 8 shows the constraints on the companion mass from the RV observations assuming these K-dwarf mass values. Both targets are consistent with massive WDs for a broad range of inclinations. However, for inclinations less than $\approx 44^\circ$ and $\approx 55^\circ$, for J1208 and J1721, respectively, the companion masses would exceed the Chandrasekhar limit and they would have to be neutron stars. If we take the limiting case and assume that the orbital inclinations are distributed uniformly in $\cos i$, this corresponds to a probability of 71 per cent and 57 per cent that J1208 and J1721 have $M_2 < 1.4\,\mathrm{M}_\odot$, respectively.

We can also determine the range of Roche-lobe filling factors $f = R_1/R_{\mathrm{RL}}$ for different values of the companion mass M_2. We estimate the Roche lobe radius R_{RL} as (Eggleton 1983)

$$\frac{R_{\mathrm{RL}}}{a} = \frac{0.49q^{-2/3}}{0.6q^{-2/3} + \ln(1+q^{1/3})}, \tag{3}$$

where a is the semimajor axis and $q = M_2/M_1$, where M_1 is the K-dwarf mass. The bottom panel of Fig. 8 shows the filling factors for the two targets. Neither are close to filling their Roche lobes ($f < 1$), suggesting there is no ongoing mass transfer.

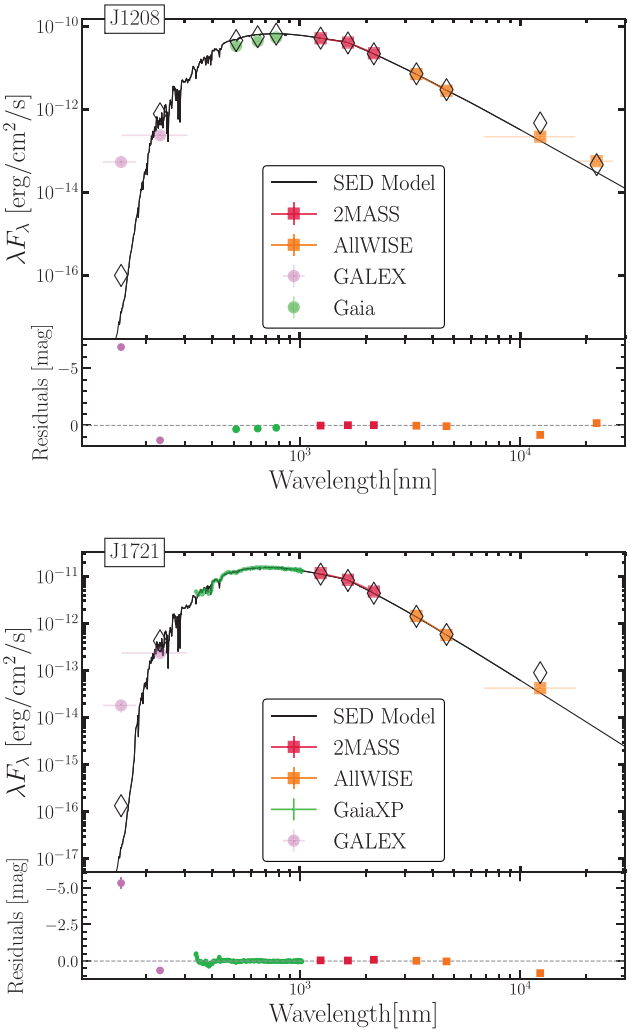

Figure 7. SEDs of J1208 (top) and J1721 (bottom) and model residuals. Both are consistent with K-dwarfs and show evidence for an FUV excess in the *GALEX* photometry. The black diamonds show the integrated fluxes predicted from the model spectrum for each filter.

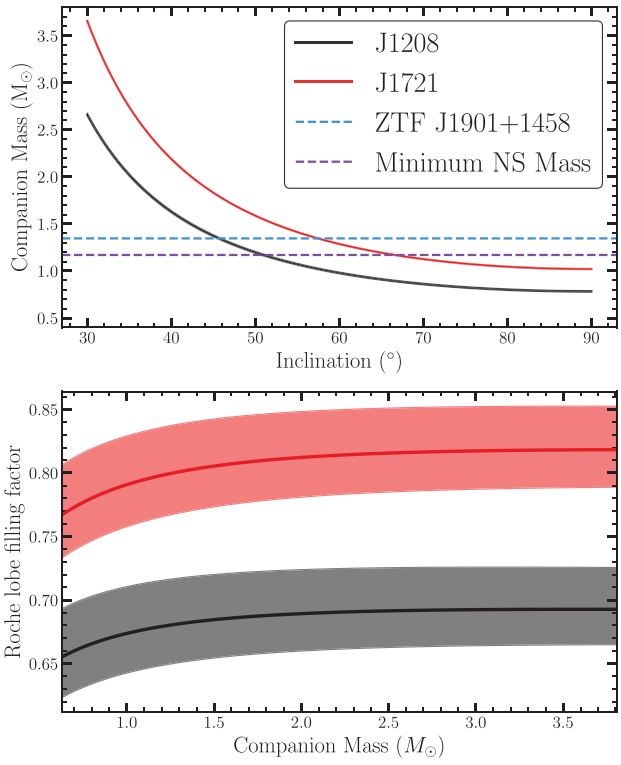

Figure 8. Top: companion mass as a function of orbital inclination for J1208 and J1721 from the RV constraints and the estimated primary mass. The shaded region shows a 0.15 $M_\odot$ uncertainty. The horizontal blue line shows the mass of the most massive known WD, ZTF J1901 + 1458 ($M = 1.35\ M_\odot$, Caiazzo et al. 2021). The purple line shows the theoretical minimum neutron star mass ($M = 1.17\ M_\odot$, Suwa et al. 2018). Bottom: Roche lobe filing factors (equation 3) for the range of M_2 in the top panel. Both targets have $f < 1$ for this range of companion masses.

4 SPOTTED ELLIPSOIDAL LIGHT-CURVE FITS

We use the *TESS* light curves to determine the orbital periods of the binary and fit spectroscopic orbits in Section 3. Ellipsoidal modulations can also be used to constrain the mass ratio and inclination of the binary when fit simultaneously with the RVs (Morris & Naftilan 1993).

Unfortunately, the light curves of J1208 and J1721 include additional variability due to spots. These vary between *TESS* sectors and introduce asymmetric maxima in the light curves, as well as departures from symmetry around conjunction. Light-curve modelling tools such as ELC (Orosz & Hauschildt 2000) and PHOEBE (Prša & Zwitter 2005; Conroy et al. 2020) can include star-spots in their light-curve models, but this has only been done for a handful of targets (e.g. Strader et al. 2019; Lin et al. 2023). These models typically do not include prescriptions for time-dependent spot evolution.

Here, we attempt to model the *TESS* light curves of J1208 and J1721 as spotted ELLs with PHOEBE to determine the mass ratio and binary inclination. However, there are degeneracies in the solutions of rotational variable light curves (Luger et al. 2021a), especially when using a single-band light curve. We fit each *TESS* sector independently, testing one- and two-spot models. We simultaneously fit the light-curve data and the RVs.

For all PHOEBE models, we treat the secondary as a dark companion by fixing it to be small, $R_2 = 3 \times 10^{-6}\ R_\odot$, and cold, $T_{\rm eff,\,2} = 300$ K. We do not include the effects of irradiation or reflection, as in Jayasinghe et al. (2022). We also fix the eccentricity $e = 0$ based on the RV fit. Each spot on the K-dwarf has an independent latitude, θ_s, longitude, ϕ_s, angular size, R_s, and temperature, T_s, parametrized as a relative temperature, $T_s/T_{\rm eff}$. The latitude is defined such that $\theta_s = 0°$ occurs at the pole corresponding to the spin axis, and $\phi_s = 0°$ corresponds to the direction facing the companion.

We start by using the differential evolution optimizer in PHOEBE to identify an initial state for the MCMC sampling. We set Gaussian priors on the effective temperature ($\sigma = 100$ K), and primary radius ($\sigma = 0.1\ R_\odot$) based on the SED fits, and a uniform prior on the primary mass ([0.5 $M_\odot$, 0.95 $M_\odot$]). We run each PHOEBE model for 10 000 iterations with 16 walkers for the one-spot models and 20 walkers for the two-spot models. We inspected the walker distributions to select suitable burn-in periods, typically 2000–5000 iterations.

Table 4 reports the MCMC posteriors for the two sectors of J1208 and Table 5 reports the results for J1721. Fig. 9 shows an example corner plot and light-curve fit for J1721 with a one-spot

Table 4. PHOEBE posteriors for J1208. We fit each sector independently and use models with one and two spots.

	S22, 1 spot	S22, 2 spot	S49, 1 spot	S49, 2 spot
Period (d)	$0.4632676^{+0.0000005}_{-0.0000005}$	$0.4632672^{+0.0000008}_{-0.0000006}$	$0.463250^{+0.000002}_{-0.000002}$	$0.463322^{+0.000003}_{-0.000003}$
T_0	$2459984.8070^{+0.001}_{-0.0009}$	$2459984.807^{+0.001}_{-0.001}$	$2459984.8073^{+0.001}_{-0.0010}$	$2459984.802^{+0.001}_{-0.001}$
q	$1.5^{+0.1}_{-0.1}$	$1.26^{+0.07}_{-0.06}$	$1.27^{+0.06}_{-0.1}$	$1.44^{+0.06}_{-0.06}$
i (°)	62^{+7}_{-4}	73^{+3}_{-3}	90^{+5}_{-5}	56^{+1}_{-1}
R_1 ($R_\odot$)	$0.77^{+0.07}_{-0.05}$	$0.74^{+0.03}_{-0.03}$	$0.66^{+0.05}_{-0.02}$	$0.73^{+0.02}_{-0.02}$
$T_{\rm eff,1}$ (K)	4710^{+80}_{-90}	4700^{+200}_{-100}	4670^{+70}_{-70}	4740^{+50}_{-50}
γ (km s^{-1})	-7^{+1}_{-3}	$-6.1^{+0.7}_{-0.6}$	-7^{+1}_{-1}	$-5.0^{+0.1}_{-0.1}$
M_1 ($M_\odot$)	$0.60^{+0.1}_{-0.08}$	$0.68^{+0.08}_{-0.07}$	$0.55^{+0.1}_{-0.04}$	$0.78^{+0.04}_{-0.05}$
M_2 ($M_\odot$)	$0.9^{+0.1}_{-0.1}$	$0.86^{+0.07}_{-0.07}$	$0.71^{+0.05}_{-0.03}$	$1.13^{+0.03}_{-0.05}$
a (au)	$0.0135^{+0.0008}_{-0.0005}$	$0.0135^{+0.0004}_{-0.0004}$	$0.0127^{+0.0005}_{-0.0002}$	$0.0146^{+0.0001}_{-0.0003}$
$\theta_{s,1}$ (°)	40^{+6}_{-4}	133^{+2}_{-2}	120^{+5}_{-5}	$75.8^{+0.8}_{-0.7}$
$\phi_{s,1}$ (°)	93^{+2}_{-1}	63^{+1}_{-2}	36^{+2}_{-1}	$315.9^{+0.3}_{-0.3}$
$R_{s,1}$ (°)	18^{+2}_{-1}	-2^{+7}_{-10}	33^{+4}_{-2}	$27.9^{+0.4}_{-0.3}$
$T_{s,1}/T_{\rm eff}$	$0.81^{+0.04}_{-0.04}$	$0.80^{+0.09}_{-0.3}$	$0.93^{+0.01}_{-0.01}$	$0.83^{+0.01}_{-0.01}$
$\theta_{s,2}$ (°)		$9.5^{+2}_{-0.8}$		$21.2^{+0.3}_{-0.2}$
$\phi_{s,2}$ (°)		98^{+2}_{-2}		$107.9^{+0.3}_{-0.4}$
$R_{s,2}$ (°)		42^{+2}_{-1}		$54.9^{+0.6}_{-0.3}$
$T_{s,2}/T_{\rm eff}$		$0.85^{+0.06}_{-0.05}$		$0.942^{+0.002}_{-0.002}$

Table 5. Same as Table 4, but for J1721.

	S12, 1 spot	S12, 2 spot	S13, 1 spot	S13, 2 spot	S39, 1 spot	S39, 2 spot
Period (d)	$0.4468^{+0.0004}_{-0.0003}$	$0.4472^{+0.0001}_{-0.0003}$	$0.4472498^{+0.0000005}_{-0.0003}$	$0.4471^{+0.0003}_{-0.0004}$	$0.446951^{+0.0003}_{-0.000001}$	$0.446637^{+0.0003}_{-0.000001}$
T_0	$2459379.536^{+0.002}_{-0.1}$	$2459379.20^{+0.2}_{-0.03}$	$2459379.3922^{+0.0006}_{-0.03}$	$2459379.18^{+0.2}_{-0.03}$	$2459379.3711^{+0.003}_{-0.0006}$	$2459379.364^{+0.003}_{-0.001}$
q	$1.62^{+0.5}_{-0.05}$	$1.95^{+0.2}_{-0.06}$	$1.9^{+0.1}_{-0.1}$	$2.24^{+0.06}_{-0.08}$	$1.92^{+0.09}_{-0.07}$	$1.36^{+0.05}_{-0.04}$
i (°)	56^{+3}_{-4}	44^{+2}_{-3}	55^{+5}_{-5}	45^{+3}_{-2}	49^{+1}_{-1}	67^{+1}_{-1}
R_1 ($R_\odot$)	$0.85^{+0.02}_{-0.05}$	$0.91^{+0.02}_{-0.03}$	$0.80^{+0.07}_{-0.03}$	$0.88^{+0.01}_{-0.01}$	$0.90^{+0.02}_{-0.02}$	$0.888^{+0.009}_{-0.008}$
$T_{\rm eff,1}$ (K)	5080^{+90}_{-50}	5110^{+90}_{-30}	5200^{+100}_{-100}	5080^{+200}_{-60}	5130^{+50}_{-70}	5040^{+50}_{-50}
γ (km s^{-1})	$-38.7^{+2}_{-0.7}$	$-39.6^{+0.2}_{-0.2}$	$-34.1^{+0.7}_{-0.8}$	$-34.0^{+0.4}_{-1}$	$-47.4^{+1}_{-0.9}$	$-40.3^{+0.2}_{-0.2}$
M_1 ($M_\odot$)	$0.84^{+0.01}_{-0.1}$	$0.88^{+0.06}_{-0.04}$	$0.73^{+0.1}_{-0.06}$	$0.86^{+0.02}_{-0.03}$	$0.70^{+0.03}_{-0.04}$	$0.838^{+0.007}_{-0.01}$
M_2 ($M_\odot$)	$1.43^{+0.1}_{-0.10}$	$1.76^{+0.09}_{-0.06}$	$1.3^{+0.3}_{-0.1}$	$1.89^{+0.08}_{-0.06}$	$1.36^{+0.06}_{-0.07}$	$1.15^{+0.04}_{-0.05}$
a (au)	$0.01491^{+0.0003}_{-0.00009}$	$0.0159^{+0.0002}_{-0.0002}$	$0.0146^{+0.0008}_{-0.0005}$	$0.0160^{+0.0002}_{-0.0001}$	$0.0146^{+0.0002}_{-0.0002}$	$0.0144^{+0.0001}_{-0.0002}$
$\theta_{s,1}$ (°)	$52.2^{+2}_{-0.4}$	$45.7^{+0.6}_{-0.8}$	$16.3^{+2}_{-0.9}$	120^{+1}_{-1}	$71.8^{+0.8}_{-0.8}$	228^{+2}_{-3}
$\phi_{s,1}$ (°)	$89.0^{+2}_{-0.9}$	89^{+1}_{-2}	$89.9^{+0.7}_{-2}$	$55.2^{+0.7}_{-0.8}$	$210.5^{+0.8}_{-0.6}$	100^{+5}_{-9}
$R_{s,1}$ (°)	$22.9^{+0.8}_{-1}$	$28.9^{+0.3}_{-1}$	29^{+2}_{-1}	$10.9^{+0.8}_{-0.8}$	$16.1^{+0.6}_{-1.0}$	19^{+2}_{-2}
$T_{s,1}/T_{\rm eff}$	$0.87^{+0.01}_{-0.01}$	$0.906^{+0.005}_{-0.01}$	$0.86^{+0.03}_{-0.01}$	$0.81^{+0.05}_{-0.06}$	$0.780^{+0.007}_{-0.008}$	$0.95^{+0.02}_{-0.01}$
$\theta_{s,2}$ (°)		$119.3^{+0.9}_{-2}$		$9.8^{+0.7}_{-0.4}$		38^{+3}_{-3}
$\phi_{s,2}$ (°)		$214.0^{+0.6}_{-2}$		$91.7^{+0.9}_{-0.8}$		198^{+2}_{-2}
$R_{s,2}$ (°)		$15.4^{+0.6}_{-2}$		$38.0^{+0.3}_{-0.4}$		$19.1^{+0.6}_{-0.9}$
$T_{s,2}/T_{\rm eff}$		$0.76^{+0.1}_{-0.04}$		$0.876^{+0.006}_{-0.01}$		$0.81^{+0.03}_{-0.02}$

model for sector 12. Fig. 10 compares the inclination, primary mass, and secondary mass posteriors for the different model fits. For both targets, we find that the models do not produce a consistent prediction for the companion mass between the *TESS* sectors and for different spot models.

4.1 PHOEBE models of J1208

The PHOEBE models of J1208 all predict unimodal posterior distributions for the orbital period, P. Three of the four PHOEBE models of J1208 predict K-dwarf masses below what is expected based on the SED with $M_1 < 0.7\,M_\odot$. While this could suggest a history of mass transfer, it seems unlikely that $\sim$0.2 $M_\odot$ of material was transferred to the WD companion. The sector 22 two-spot model also finds a spot size consistent with zero for one of the spots ($R_s = -2^{+7^\circ}_{-10^\circ}$), which may suggest a one-spot model is preferable for that sector. However, we note that the position and size of the spot differs between the two models (Table 4).

We can also compare the predicted spot temperatures to expectations based on analytic models from Berdyugina (2005), where the

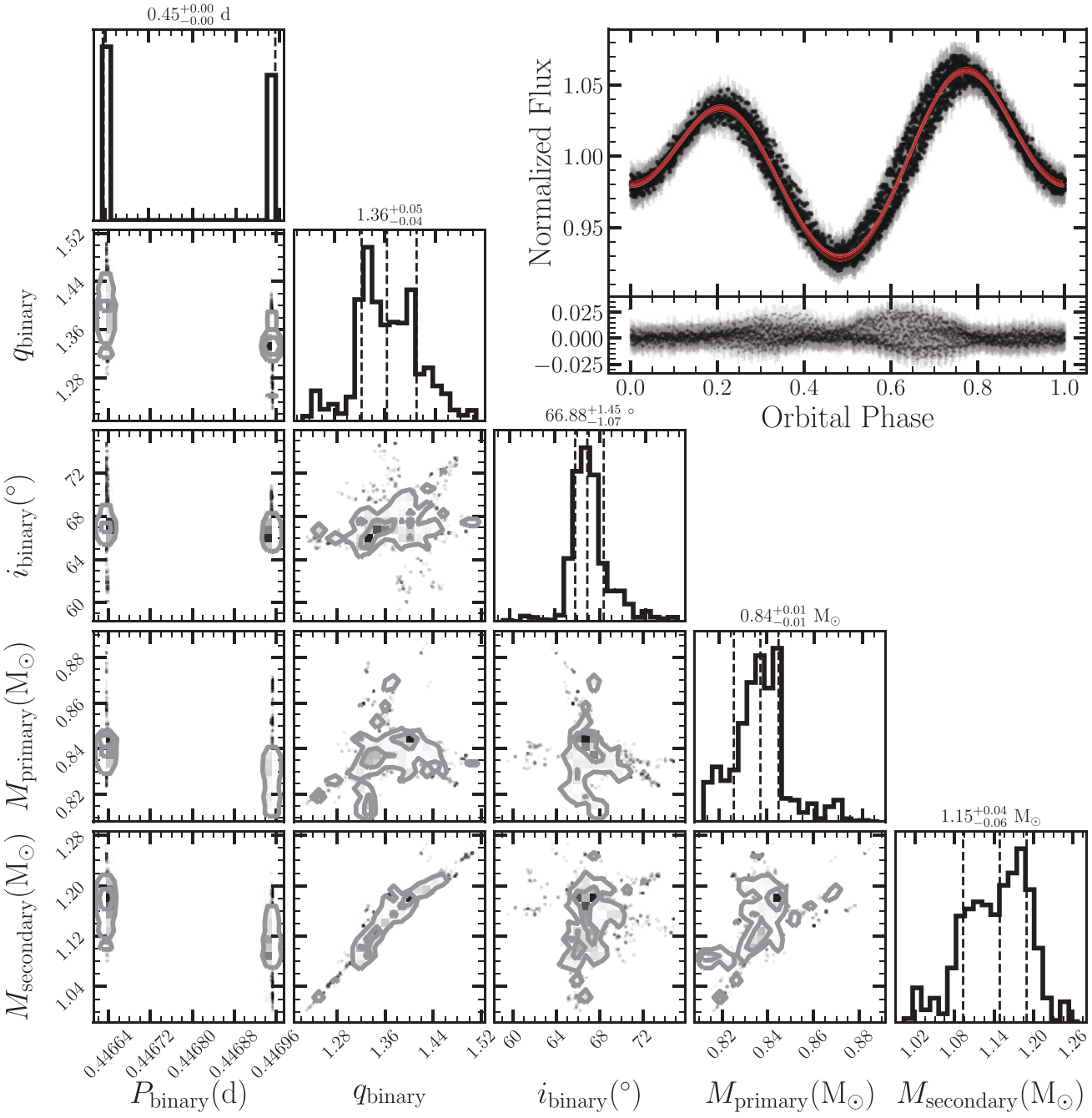

Figure 9. MCMC posteriors for the sector 39 two-spot model of J1721. The light-curve fit and residuals are shown in the upper right. This model predicts a companion mass consistent with a massive WD.

spot temperature T_s is related to the effective temperature by

$$T_s = -895\left(\frac{T_{\rm eff}}{5000\ {\rm K}}\right)^2 + 3755\left(\frac{T_{\rm eff}}{5000\ {\rm K}}\right) + 808\ {\rm K}. \quad (4)$$

Based on the effective temperature from the SED (4700 K), the spot temperature is predicted to be 3545 K, which corresponds to a ratio $T_s/T_{\rm eff} = 0.75$. This value is lower than the MCMC results for all models. This could indicate that this target has an atypically low contrast between the spot and the photosphere, or that a more complex spot model is necessary for J1208.

The two models for sector 49 predict significantly different inclinations ($90^{+5^\circ}_{-5^\circ}$ and $56^{+1^\circ}_{-1^\circ}$), so it is not surprising the spot parameters are not consistent between the one- and two-spot models. The spot in the sector 49 one-spot model is much hotter than in the sector 22 models, $T_{s,1}/T_{\rm eff} = 0.93^{+0.01}_{-0.01}$, and the second spot in the sector 49 two-spot model is similarly hot.

The sector 49 two-spot model predicts a higher primary mass ($M_1 = 0.78^{+0.04}_{-0.05}$ M$_\odot$) and a higher mass ratio, $q = 1.44^{+0.06}_{-0.06}$. The result is a much larger WD mass, $M_2 = 1.13^{+0.03}_{-0.05}$ M$_\odot$. While it is tempting to prefer this model because of the better agreement with the SED mass and radius, it is clear that there are numerous degeneracies in the light-curve solutions that limit our ability to characterize the WD.

The sector 49 one-spot model also predicts an edge-on inclination, $i = 90 \pm 5^\circ$. We might expect to be able to rule this model out based

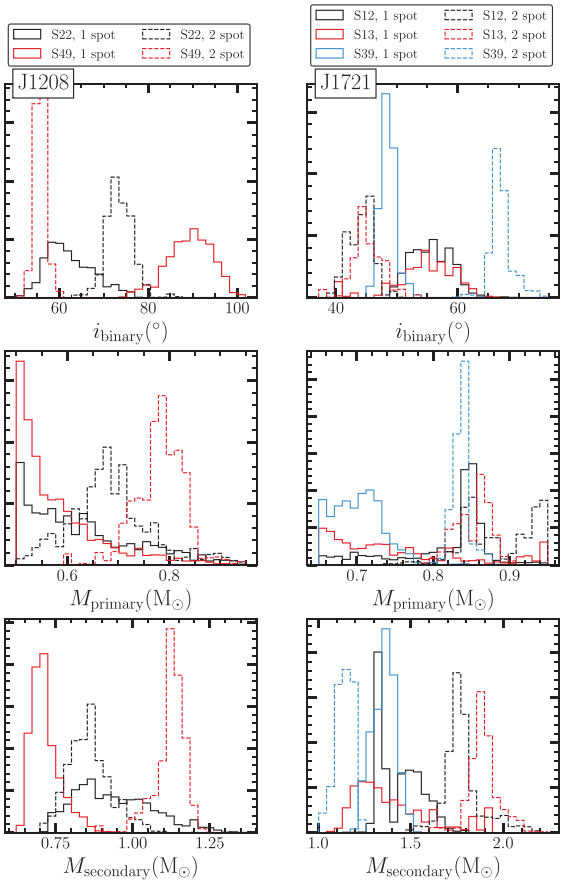

Figure 10. MCMC posteriors for J1208 (left) and J1721 (right). We find that the different sectors and number of spots produces variable predictions of the orbital inclination and secondary mass.

on the lack of an eclipse. Using the non-relativistic WD scaling relation $R \propto M^{-1/3}$, a WD mass of $M_2 = 0.71\,\rm M_\odot$ should have a radius $R_2 \approx 0.95\,\rm R_\oplus$. Fig. 11 shows the best-fitting PHOEBE model after changing R_2 to be consistent with a WD of a few Earth radii. The scatter around the model primarily comes from the evolution of the spot across the *TESS* sector. Although we can plausibly rule out a companion of radius $R_2 = 5\,\rm R_\oplus$, we would not expect to detect eclipses of companions $R_2 \sim 1\,\rm R_\oplus$ and therefore cannot place an upper limit on the inclination.

4.2 PHOEBE models of J1721

Unlike J1208, the PHOEBE models of J1721 all have multimodal posterior distributions for the orbital period, P. The difference between the periods is small, typically 15–45 min. This could come from slightly asynchronous rotation, where the orbital period does not equal the rotation period, or latitudinal differential rotation in the K-dwarf. Similar differences were found between the orbital period and photometric period of the G + WD binary CPD-65 264 (Hernandez et al. 2022b).

For J1721, the secondary mass posteriors span from 1 to 1.9 $\rm M_\odot$ depending on the sector and number of spots. For the sectors 13 and 39 single-spot models, the primary mass posterior is lower than what is expected from the SED. The two-spot model for sector 12 predicts a primary mass at the upper range of our mass prior, $\sim$0.95 $\rm M_\odot$. The two-spot models for sectors 13 and 39 predict primary masses consistent with our expectations from the CMD,

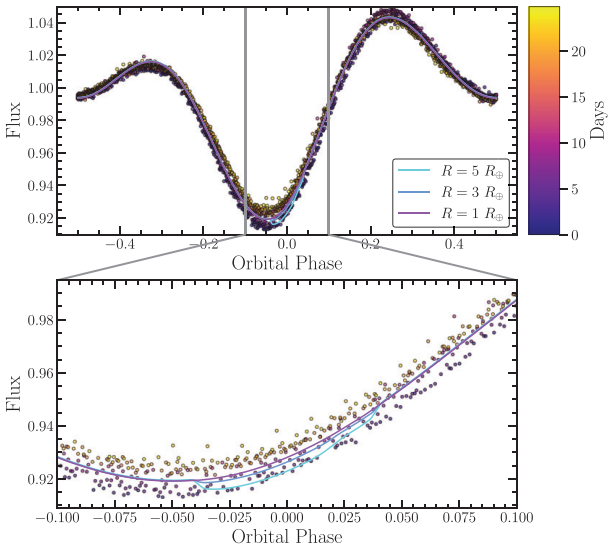

Figure 11. The PHOEBE sector 49 one-spot model shown for different WD radii. The sector 49 one-spot model (Table 4) prefers an edge-on inclination and a WD mass that corresponds to a radius $R_2 \approx 0.95\,\rm R_\oplus$ based on WD scaling relation. However, we are unable to confirm or reject this model on the basis of eclipse detection, in part due to the scatter in the model from the spot modulation throughout the *TESS* sector. To centre the eclipse feature at phase $\phi = 0$, orbital phase is defined such that RV maxima occurs at $\phi = -0.25$ in this figure.

but yield discrepant inclinations $45^{+3}_{-2}{}^\circ$ and $67^{+1}_{-1}{}^\circ$, respectively. The sector 13 model then predicts a companion with $M_2 = 1.89^{+0.08}_{-0.06}\,\rm M_\odot$, consistent with a neutron star companion, while sector 39 model predicts $M_2 = 1.15^{+0.04}_{-0.05}\,\rm M_\odot$, consistent with a massive WD.

In comparing the spot parameters for these two models, the sector 13 two-spot model predicts two spots of different angular sizes with similar temperatures. The sector 39 two-spot model predicts two spots of the same size, but with different temperatures. Since the spots evolve, it is not surprising that the positions and sizes of the spots are different, especially since the two sectors are separated by almost two years. As with J1208, the posterior spot temperature ratio is higher than what is predicted from the analytic model, $T_s/T_{\rm eff} = 0.73$.

Unlike J1208, where the two *TESS* sectors are separated by $\sim$2 yr, J1721 was observed in two consecutive sectors (12 and 13). The light curves of these two sectors are similar, with the sector 13 observations showing a higher second maxima. In the one-spot models of these two sectors, the effective temperature of the spots are similar, but the size increases going from sector 12 to sector 13. Models of both sectors prefer an inclination $\sim$55°, and the spots in the two models appear at similar longitudes. The sector 13 spot prefers a lower latitude.

In comparing the two-spot models of sectors 12 and 13, we see that spot one of the sector 12 model shares a similar longitude and temperature with spot two of the sector 13 model, though it appears at a different latitude and gets larger by $\sim$10°. Alternatively, the second spot of the sector 12 model appears at a similar latitude to the first spot of the sector 13 model, but with different longitude and a decreasing size $\sim$4.5°. An important caveat with the two-spot models of sectors 12 and 13 is that one of the spots (spot two of sector 12 and spot one of sector 13) appears at a latitude $\sim$120°, which is not visible to the observer in the plane of the sky given the orbital inclination. These spots therefore contribute negligibly to the light curve. This may indicate a preference for the one-spot model. While these models may offer insight into the magnetic fields of

chromospherically active close binaries, there is no reason to prefer a model with two spots over a model with more spots.

In summary, the light curves of both targets show ellipsoidal modulations with additional variability due to spots. Since the spots evolve over time, the *TESS* light-curve morphology changes between sectors. We attempt to use PHOEBE to model the light curves using one and two-spot models, but degeneracies with spot parameters limit our ability to characterize the systems. In light of these results, we also perform an injection-recovery test for a synthetic spotted binary in Appendix A. Although we only test one synthetic binary, we do not recover the injected spot parameters or orbital inclinations. We therefore do not report final measurements of the companion mass M_2 from the PHOEBE models.

5 DISCUSSION

The *TESS* light curves, RV observations, and SEDs suggest that J1208 and J1721 are K-dwarf binaries with massive WD companions. Whereas the majority of WD + main sequnce (MS) binaries have M-dwarf stars, J1208 and J1721 have K-dwarf photometric primaries, of which there are relatively few systems known (Wonnacott et al. 1993; Zheng et al. 2022; Hernandez et al. 2022b). Both systems have large RV amplitudes and have magnitudes and colours consistent with a single-star isochrone (Fig. 2). The *TESS* light curves show periodic variability at ∼0.45 d. The light-curve morphology changes dramatically between *TESS* sectors (Fig. 3) due to the combination of ellipsoidal variability and star-spots.

We obtain RV observations of these targets using APF, PEPSI, and CHIRON (Tables 2 and 3). The spectroscopic orbits (Fig. 5) imply mass functions $f(M) = 0.20$ and $0.30\,M_\odot$ for J1208 and J1721, respectively. We then use SEDs to estimate the primary mass of each target (Fig. 7), which can be used to place broad constraints on the companion mass (Fig. 8), suggesting that these are massive WDs.

There are also some key differences between the two targets. J1208 has a more significant FUV excess and an X-ray detection. The X-ray to bolometric luminosity ratio is consistent with what is expected from chromospheric activity. This target also shows evidence of Hα emission (Fig. 6) and long-term photometric variability (Fig. 4), neither of which are observed for J1721. It could be the case that J1208 is more chromospherically active, or that J1721 is in a low activity state.

Our ability to characterize the unseen companion using RVs is limited by the unknown orbital inclination. We attempt to model the *TESS* light curves using PHOEBE to estimate the inclination, treating each sector independently and using one- and two-spot models. We find that the models do not predict a consistent orbital inclination and secondary mass between sectors, presumably due to degeneracies in modelling the light curves of spotted stars using a single photometric band.

The J1208 PHOEBE models generally prefer a low-mass photometric primary that is not consistent with the SED $T_{\rm eff}$ or radius. It would be better to simultaneously fit the SED with the light curves and RVs, but this is beyond the current capabilities of PHOEBE. Models of the binary evolution history could also be used to place constraints on the amount of mass that could be transferred from the K-dwarf. The J1721 PHOEBE models predict a range of companion masses, including some $>1.4\,M_\odot$ consistent with a neutron star companion. However, like J1208, the estimates of the primary mass do not match the expectations from the SED, making interpretation of these models challenging.

Simultaneous multiband light curves could be used to break some of the degeneracies in the light curves of rotational variability (Luger et al. 2021a). We are ultimately less interested in determining the spot parameters than in determining the orbital inclination and mass ratio, so Gaussian processes may provide a pathway to handling spot evolution and fitting multiple *TESS* sectors simultaneously (e.g. Luger, Foreman-Mackey & Hedges 2021b). Since J1721 was observed in two consecutive sectors, this target may be a good test case for time-dependent models. UV spectroscopy seems to be the most promising approach to better constrain the nature of the companions, particularly to discriminate between neutron stars and WDs. For example, Hernandez et al. (2022b) characterized the WD companion ($M = 0.86 \pm 0.06\,M_\odot$) to a G-dwarf using *HST* UV spectroscopy. Similar observations of J1208 and J1721 could provide additional constraints on the compact object companions.

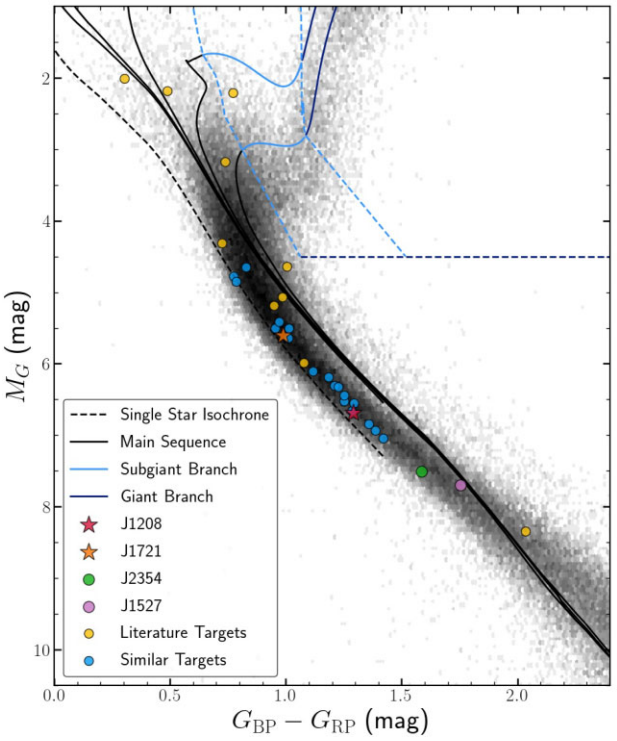

Figure 12. *Gaia* CMD of our targets (J1208 and J1721) compared to similar targets identified in the literature (green). The solid black line shows a binary isochrone corresponding to an equal mass binary. We also identify a number of systems listed in Table 6 with similar light curves and high *Gaia* $A_{\rm RV}$ shown in blue.

We might also expect the kinematics of WD and neutron star binaries to differ. Neutron stars are expected to experience natal kicks following the supernova that can affect their subsequent motion through the Galaxy. X-ray binaries with neutrons stars have been found to have Galactic kinematics significantly different from 'normal' stars (e.g. González Hernández et al. 2005). Natal kicks are expected to be ≈ 50 per cent larger for neutron stars than black holes (Atri et al. 2019; O'Doherty et al. 2023), and we may expect J1208 and J1721 to have atypical Galactic orbits if they host a neutron star companion. We use the *Gaia* DR3 parallax, proper motion, and the centre-of-mass velocity from the RVs to estimate the trajectory of J1208 and J1721 in the Galaxy. We use `galpy` (Bovy 2015) and the `MWPotential2014` potential to integrate the orbits from 500 Myr ago to 500 Myr in the future. Both orbits are consistent with the thin disc, staying ≲ 200 pc from the Galactic mid-plane (Du et al. 2006).

In recent years, there have been a number of candidate non-interacting compact objects identified based on the photometric

Table 6. Targets with similar CMD positions, light curves identified through *Gaia* and *TESS* in Section 5. M_G and $G_{BP} - G_{RP}$ report the extinction-corrected absolute magnitude and colour, respectively. The mass function $f(M)$ is computed using the photometric period and treating $A_{RV} = 2K$. For targets identified in previous work, we instead use the reported RV semi-amplitude, K, when available, to compute $f(M)$.

GDR3 source	Period (d)	Distance (pc)	G (mag)	M_G (mag)	$G_{BP} - G_{RP}$ (mag)	A_{RV} (km s^{-1})	K (km s^{-1})	$f(M)$ ($M_\odot$)	Reference
5379221348814190336	0.244329	211.462952	12.224591	5.502547	1.014184	265.22	–	0.06	–
538 490565647002752	0.254756	309.284088	12.865199	4.773744	0.773373	96.14	–	<0.01	–
888901687304620416	0.271789	138.248932	12.638993	6.935684	1.386844	165.28	–	0.02	–
386667182582 268928	0.336922	160.036407	12.571529	6.550435	1.293825	212.38	–	0.04	–
124151875142913152	0.375076	245.143860	12.907320	5.417380	0.971541	218.40	–	0.05	–
421818053 931122176	0.381958	189.259827	12.824433	6.439141	1.252892	50.08	–	<0.01	–
806594102274873344	0.501581	143.932281	12.098151	6.307360	1.208750	108.31	–	0.01	–
3717122881328373632	0.516191	75.350815	10.570268	6.184828	1.185923	68.08	–	<0.01	–
2990513370894699392	0.576676	127.991974	11.857308	6.321394	1.227760	68.91	–	<0.01	–
17904898 318 910080	0.588986	205.427795	12.616076	5.502595	0.954732	108.53	–	0.01	–
4831037389874593920	0.696708	172.845840	13.052012	6.845022	1.358981	291.35	–	0.22	–
1842647931849558272	0.745748	159.734238	12.678954	6.661964	1.284475	87.85	–	0.01	–
517420310786820352	1.013753	265.975525	12.696167	4.852485	0.786578	296.93	–	0.34	–
65626554825500672	1.684941	204.862473	12.596542	5.637171	1.011639	50.10	–	<0.01	–
5570313476125894528	1.739302	388.706482	12.696926	4.650250	0.826697	259.00	–	0.39	–
5702192817771804416	1.859799	169.964844	12.256246	6.104451	1.118523	348.88	–	1.02	–
2052252132725589888	2.543089	192.014145	12.969660	6.520600	1.252131	75.75	–	0.01	–
2809553337714753920	5.678659	133.043991	12.657634	7.037658	1.420611	51.90	–	0.01	–
Literature targets:									
1375051479376039040	0.256	117.975426	13.054289	7.695331	1.754247	358.05	$171.09^{+1.0}_{-0.97}$	0.131 ± 0.002	Lin et al. (2023)
1542461401838152960	0.273	352.493530	12.799067	5.063311	0.986489	726.78	–	1.36	Fu et al. (2022)
770431444010267392	0.274	314.473907	15.832041	8.344118	2.035088	–	257.0 ± 2.0	0.48 ± 0.01	Yi et al. (2022)
5687390848640176000	0.450	363.837830	12.505296	4.637274	1.005107	590.24	–	1.20	Fu et al. (2022)
2874966759081257728	0.480	127.261543	13.025951	7.502465	1.585217	458.46	219.4 ± 0.5	0.525 ± 0.004	Zheng et al. (2023)
1633051023841345280	0.600	229.506454	12.942164	5.990063	1.078550	–	$124.4^{+1.0}_{-1.1}$	0.120 ± 0.003	Zheng et al. (2022)
3379200833078092672	0.693	2798.946040	14.544648	2.013422	0.302947	–	133.22 ± 0.47	0.170 ± 0.002	Qi et al. (2023)
608189290627289856	0.790	324.910400	12.767137	5.187158	0.948391	347.97	$128.4^{+0.84}_{-0.73}$	0.17	Li et al. (2022)
3381426828726340992	1.229	1327.539920	13.892116	3.171073	0.737637	–	99.1 ± 0.64	0.124 ± 0.002	Qi et al. (2023)
4672702561514172544	1.370	205.238098	10.964239	4.312936	0.725459	202.09	100.83 ± 0.09	0.1456 ± 0.0004	Hernandez et al. (2022b)
3381441465975139968	2.91	2246.095210	13.958452	2.180150	0.488671	–	67.18 ± 0.4	0.092 ± 0.002	Qi et al. (2023)
66844160873323008	3.929	841.156189	12.240489	2.214047	0.770942	133.35	61.72 ± 0.3	0.096 ± 0.001	Qi et al. (2023)

and RV variability of late-type stars. Zheng et al. (2023) reported LAMOST J235456.76 + 335625.7 (J2354) as a nearby neutron star candidate with mass $M_2 > 1.26 \pm 0.03\,M_\odot$. Like J1208 and J2354, this binary has an orbital period $P = 0.47991$ d and a light curve dominated by spotted ellipsoidal variability in *TESS* observations. J2354 also has a significant *GALEX* NUV excess and an Hα emission line that traces the motion of the K-dwarf. While Zheng et al. (2023) propose that the companion to J2354 is a neutron star, the system also may be a massive WD (Tucker et al., in preparation).

Lin et al. (2023) also reported the detection of a similar system 2MASS J15274848 + 3536572 (J1527) using LAMOST RVs. The orbital period is shorter, with $P = 0.256$ d, and they find that the K9-M0 primary has a mass $M_1 = 0.62 \pm 0.01\,M_\odot$. The light curve is again similar to J1208, J1721, and J2354, and appears to show similar modulations over time. The mass function of J1527 is $f(M) = 0.131 \pm 0.002\,M_\odot$. They also attempt a PHOEBE fit to the *B*, *V*, *R*, and *TESS* light curves, and report $M_2 = 0.98 \pm 0.03\,M_\odot$. Unlike J1208 and J2354, the Hα emission moves in antiphase with the photometric primary, which could indicate the presence of an accretion disc. If the companion is instead a neutron star, the lack of X-ray and γ-ray detection suggests it is part of the X-ray dim NS population. A neutron star with $M = 0.98\,M_\odot$ challenges our understanding of core-collapse supernovae, which are expected to yield remnants with minimum masses $\sim$1.17 $M_\odot$ (Suwa et al. 2018). A more recent re-analysis of this system has suggested that the companion is actually a WD with $M = 0.69\,M_\odot$ (Zhang et al. 2024).

Fig. 12 shows these systems on a *Gaia* CMD. Similar targets have also been identified in Li et al. (2022), Qi et al. (2023), Fu et al. (2022), Zheng et al. (2022), Hernandez et al. (2022b), and Yi et al. (2022), though some do not have evidence of rotational variability in their light curves. Some of these sources appear more luminous than expected for a single main-sequence star. Spectra of these targets are needed to rule out a second luminous component.

If many of these objects turn out to be massive WDs, rather than luminous companions, this could have implications for the overall mass distribution of WDs. J1208, J1721, J2354 (Zheng et al. 2023), and J1527 (Lin et al. 2023) are all within 250 pc using *Gaia* distances (Bailer-Jones et al. 2021). The local density of K-dwarfs with massive WD companions is then at least $\rho_\odot = 3N/4\pi R^3 \sim 6.1 \times 10^{-8}$ pc^{-3}. For a simple thin disc model normalized by this density with

$$\rho = \rho_\odot \exp\left(-(R - R_s)/R_d - |z|/h\right), \quad (5)$$

where $R_d = 3500$ pc is the disc scale length, $R_\odot$, $R_s = 8500$ pc is the radius of the Sun from the Galactic centre, z is the distance from the Galactic mid-plane, and $h = 150$ pc is the disc height, we can estimate that there are $\gtrsim$ 16 000 such systems the Galaxy. This is far fewer than the number of NS expected in the Galaxy ($\sim 10^8$–10^{10}, Sartore et al. 2010) and complicates the discrimination between NS and massive WD companions from a statistical perspective.

Finally, we also performed a simple search to identify other systems which may contain similar companions. We start by selecting stars with *Gaia* $A_{RV} > 50$ km s^{-1}, and $G < 15$ mag that were flagged as photometric variables in *Gaia* DR3. We also require that the *Gaia* parallax error satisfies $\varpi/\sigma_\varpi > 5$ and that the *V*-band extinction is $A_V < 2.0$ mag. We then use the extinction-corrected *Gaia* CMD to select stars that appear more consistent with a single main-sequence star than a stellar binary. We do this by selecting targets fainter than a single star isochrone increased in luminosity by a factor of 1.5 (0.44 mag). These selection criteria yield 826 targets in the absolute magnitude range $4.5 < M_G < 12$ mag. We then visually inspected their *TESS* QLP light curves, when available, selecting systems with similar orbital periods and ELL/spotted ELL light curves. In total, we identified 18 targets, which are shown in Fig. 12 and listed in Table 6.

Table 6 also includes estimates of $f(M)$ using the photometric period and assuming $K = A_{RV}/2$. While this may be useful as a way to prioritize targets, A_{RV} is overestimated for our two targets. We find $K \simeq 0.44 A_{RV}$ and $\simeq 0.2 A_{RV}$ for J1208 and J1721, respectively. RV observations of the targets in Table 6 are needed to identify luminous companions and constrain the binary mass function. It is likely that some of these objects are similar to the two targets described here or to the previous reported WD/NS candidates.

J1208 and J1721 join a small population of FGK stars with massive WD companions. As compared to WD+M stars, there are relatively few WD+FGK binaries since the main-sequence star outshines the WD at optical wavelengths. Spectroscopic orbits are promising tools to identify and characterize WD + K binaries. However, these searches are likely biased towards systems with large companion mass where the velocity semi-amplitude is large enough to rule out luminous companions. Upcoming spectroscopic missions such Milky Way Mapper (Kollmeier et al. 2017) and future *Gaia* data releases are expected to expand the sample of WD + FGK binaries.

ACKNOWLEDGEMENTS

We thank the PHOEBE developers for their support in implementing various light-curve models and the anonymous reviewer whose comments helped improve the quality and clarity of this manuscript. We thank Las Cumbres Observatory and its staff for their continued support of ASAS-SN. ASAS-SN is funded in part by the Gordon and Betty Moore Foundation through grants GBMF5490 and GBMF10501 to the Ohio State University, and also funded in part by the Alfred P. Sloan Foundation grant G-2021-14192.

This work presents results from the European Space Agency space mission *Gaia*. *Gaia* data are being processed by the Gaia Data Processing and Analysis Consortium (DPAC). Funding for the DPAC is provided by national institutions, in particular the institutions participating in the Gaia MultiLateral Agreement.

This paper includes data collected with the *TESS* mission, obtained from the MAST data archive at the Space Telescope Science Institute (STScI). Funding for the *TESS* mission is provided by the NASA Explorer Program. STScI is operated by the Association of Universities for Research in Astronomy, Inc., under NASA contract NAS 5–26555. CSK and DMR TESS research is supported by NASA grant 80NSSC22K0128.

Support for TJ and DVM was provided by NASA through the NASA Hubble Fellowship grants HF2-51509 and HF2-51464 awarded by the Space Telescope Science Institute, which is operated by the Association of Universities for Research in Astronomy, Inc., for NASA, under contract NAS5-26555. CYL acknowledges support from NASA FINESST grant no. 80NSSC21K2043 and a research grant from the H2H8 Foundation.

The LBT is an international collaboration among institutions in the United States, Italy, and Germany. LBT Corporation partners are: The University of Arizona on behalf of the Arizona Board of Regents; Istituto Nazionale di Astrofisica, Italy; LBT Beteiligungsgesellschaft, Germany, representing the Max-Planck Society, The Leibniz Institute for Astrophysics Potsdam, and Heidelberg University; The Ohio State University, representing OSU, University of Notre Dame, University of Minnesota, and University of Virginia. PEPSI was made possible by funding through the State of Brandenburg (MWFK) and the German Federal Ministry of Education and Research (BMBF) through their Verbundforschung grants 05AL2BA1/3 and 05A08BAC.

DATA AVAILABILITY

The *Gaia* DR3 data and the ASAS-SN and *TESS* light curves are all publicly available.

The ASAS-SN photometric data underlying this article are available in the the ASAS-SN Photometry Database (https://asas-sn.osu.edu/photometry). The data underlying this article are available in the article and in its online Supporting Information.

REFERENCES

Afşar M., Ibanoğlu C., 2008, MNRAS, 391, 802
Andrews J. J., Breivik K., Chatterjee S., 2019, ApJ, 886, 68
Atri P. et al., 2019, MNRAS, 489, 3116
Bailer-Jones C. A. L., Rybizki J., Fouesneau M., Demleitner M., Andrae R., 2021, AJ, 161, 147
Berdyugina S. V., 2005, Living Rev. Solar Phys., 2, 8
Bianchi L., Shiao B., Thilker D., 2017, ApJS, 230, 24
Blanco-Cuaresma S., 2019, MNRAS, 486, 2075
Blanco-Cuaresma S., Soubiran C., Heiter U., Jofré P., 2014, A&A, 569, A111
Blomme R. et al., 2023, A&A, 674, A7
Bovy J., 2015, ApJS, 216, 29
Bovy J., Rix H.-W., Green G. M., Schlafly E. F., Finkbeiner D. P., 2016, ApJ, 818, 130
Breivik K., Chatterjee S., Larson S. L., 2017, ApJ, 850, L13
Caiazzo I. et al., 2021, Nature, 595, 39
Camisassa M. E. et al., 2019, A&A, 625, A87
Castelli F., Kurucz R. L., 2003, in Piskunov N., Weiss W. W., Gray D. F., eds, Proc. IAU Symp. 210, Modelling of Stellar Atmospheres. Astron. Soc. Pac., San Francisco, p. A20
Catalán S., Isern J., García-Berro E., Ribas I., 2008, MNRAS, 387, 1693
Chakrabarti S. et al., 2023, AJ, 166, 6
Choi J., Dotter A., Conroy C., Cantiello M., Paxton B., Johnson B. D., 2016, ApJ, 823, 102
Conroy K. E. et al., 2020, ApJS, 250, 34
Cropper M. et al., 2018, A&A, 616, A5
Cui X.-Q. et al., 2012, Res. Astron. Astrophys., 12, 1197
Cummings J. D., Kalirai J. S., Tremblay P. E., Ramirez-Ruiz E., Choi J., 2018, ApJ, 866, 21
Cutri R. M. et al., 2003, 2MASS All Sky Catalog of point sources.. NASA/IPAC Infrared Science Archive
Cutri R. M. et al., 2012, VizieR Online Data Catalog, p. II/311
De Angeli F. et al., 2023, A&A, 674, A2
De Marco O., Passy J.-C., Moe M., Herwig F., Mac Low M.-M., Paxton B., 2011, MNRAS, 411, 2277
Dotter A., 2016, ApJS, 222, 8
Drimmel R., Cabrera-Lavers A., López-Corredoira M., 2003, A&A, 409, 205
Du C., Ma J., Wu Z., Zhou X., 2006, MNRAS, 372, 1304
Eggleton P. P., 1983, ApJ, 268, 368
El-Badry K., Seeburger R., Jayasinghe T., Rix H.-W., Almada S., Conroy C., Price-Whelan A. M., Burdge K., 2022, MNRAS, 512, 5620
El-Badry K. et al., 2023, MNRAS, 518, 1057
Eyer L. et al., 2023, A&A, 674, A13
Foreman-Mackey D., Hogg D. W., Lang D., Goodman J., 2013, PASP, 125, 306
Fu J.-B., Gu W.-M., Zhang Z.-X., Yi T., Qi S.-Y., Zheng L.-L., Liu J., 2022, ApJ, 940, 126
Gaia Collaboration, 2016, A&A, 595, A1
Gaia Collaboration, 2023, A&A, 674, A1
Giles H. A. C., Collier Cameron A., Haywood R. D., 2017, MNRAS, 472, 1618
González Hernández J. I., Rebolo R., Peñarrubia J., Casares J., Israelian G., 2005, A&A, 435, 1185
Green G. M., Schlafly E., Zucker C., Speagle J. S., Finkbeiner D., 2019, ApJ, 887, 93
Green M. J., Maoz D., Mazeh T., Faigler S., Shahaf S., Gomel R., El-Badry K., Rix H.-W., 2023, MNRAS, 522, 29
Hart K. et al., 2023, preprint (arXiv:2304.03791)
Hernandez M. S. et al., 2021, MNRAS, 501, 1677
Hernandez M. S. et al., 2022a, MNRAS, 512, 1843
Hernandez M. S. et al., 2022b, MNRAS, 517, 2867
Howard A. W. et al., 2010, ApJ, 721, 1467
Huang C. X. et al., 2020a, Res. Notes Am. Astron. Soc., 4, 204
Huang C. X. et al., 2020b, Res. Notes Am. Astron. Soc., 4, 206
Ivanova N. et al., 2013, A&AR, 21, 59
Jayasinghe T. et al., 2022, MNRAS, 516, 5945
Jayasinghe T., Rowan D. M., Thompson T. A., Kochanek C. S., Stanek K. Z., 2023, MNRAS, 521, 5927
Kiraga M., Stępień K., 2013, Acta Astron., 63, 53
Kochanek C. S. et al., 2017, PASP, 129, 104502
Kollmeier J. A. et al., 2017, preprint (arXiv:1711.03234)
Li X., Wang S., Zhao X., Bai Z., Yuan H., Zhang H., Liu J., 2022, ApJ, 938, 78
Lin J. et al., 2023, ApJ, 944, L4
Loeb A., Gaudi B. S., 2003, ApJ, 588, L117
Lomb N. R., 1976, Ap&SS, 39, 447
Luger R., Foreman-Mackey D., Hedges C., Hogg D. W., 2021a, AJ, 162, 123
Luger R., Foreman-Mackey D., Hedges C., 2021b, AJ, 162, 124
Marshall D. J., Robin A. C., Reylé C., Schultheis M., Picaud S., 2006, A&A, 453, 635
Martin J., Fuhrmeister B., Mittag M., Schmidt T. O. B., Hempelmann A., González-Pérez J. N., Schmitt J. H. M. M., 2017, preprint (arXiv:1708.04895)
Masuda K., Hotokezaka K., 2019, ApJ, 883, 169
Mignon L. et al., 2023, A&A, 675, A168
Morris S. L., Naftilan S. A., 1993, ApJ, 419, 344
Mu H.-J. et al., 2022, Sci. China Phys. Mech. Astron., 65, 229711
O'Doherty T. N., Bahramian A., Miller-Jones J. C. A., Goodwin A. J., Mandel I., Willcox R., Atri P., Strader J., 2023, MNRAS, 521, 2504
Orosz J. A., Hauschildt P. H., 2000, A&A, 364, 265
Paczynski B., 1976, in Eggleton P., Mitton S., Whelan J., eds, Proc. IAU Symp. 73, Structure and Evolution of Close Binary Systems. D. Reidel Publishing Co., Dordrecht,, p. 75
Parsons S. G. et al., 2015, MNRAS, 452, 1754
Pizzolato N., Maggio A., Micela G., Sciortino S., Ventura P., 2003, A&A, 397, 147
Pojmanski G., 1997, Acta Astron., 47, 467
Politano M., van der Sluys M., Taam R. E., Willems B., 2010, ApJ, 720, 1752
Prša A., Zwitter T., 2005, ApJ, 628, 426
Qi S., Gu W.-M., Yi T., Zhang Z.-X., Wang S., Liu J., 2023, AJ, 165, 187
Rebassa-Mansergas A., Gänsicke B. T., Schreiber M. R., Koester D., Rodríguez-Gil P., 2010, MNRAS, 402, 620
Ricker G. R. et al., 2015, J. Astron. Telesc. Instrum. Syst., 1, 014003
Röpke F. K., De Marco O., 2023, Living Rev. Comput. Astrophys., 9, 2
Roulston B. R., Green P. J., Kesseli A. Y., 2020, ApJS, 249, 34
Rowan D. M., Stanek K. Z., Jayasinghe T., Kochanek C. S., Thompson T. A., Shappee B. J., Holoien T. W. S., Prieto J. L., 2021, MNRAS, 507, 104
Sandquist E. L., Taam R. E., Chen X., Bodenheimer P., Burkert A., 1998, ApJ, 500, 909
Sartore N., Ripamonti E., Treves A., Turolla R., 2010, A&A, 510, A23
Scargle J. D., 1982, ApJ, 263, 835
Schwab C., Spronck J. F. P., Tokovinin A., Szymkowiak A., Giguere M., Fischer D. A., 2012, in McLean I. S., Ramsay S. K., Takami H., eds, Proc. SPIE Conf. Ser. Vol. 8446, Ground-based and Airborne Instrumentation for Astronomy IV. SPIE, Bellingham, p. 84460B
Shappee B. J. et al., 2014, ApJ, 788, 48
Strader J. et al., 2019, ApJ, 872, 42
Strassmeier K. G. et al., 2015, Astron. Nachr., 336, 324
Suwa Y., Yoshida T., Shibata M., Umeda H., Takahashi K., 2018, MNRAS, 481, 3305
Swihart S. J., Strader J., Chomiuk L., Aydi E., Sokolovsky K. V., Ray P. S., Kerr M., 2022, ApJ, 941, 199
Tanikawa A., Hattori K., Kawanaka N., Kinugawa T., Shikauchi M., Tsuna D., 2023, ApJ, 946, 79

Tokovinin A., Fischer D. A., Bonati M., Giguere M. J., Moore P., Schwab C., Spronck J. F. P., Szymkowiak A., 2013, PASP, 125, 1336
Voges W. et al., 1999, A&A, 349, 389
Vogt S. S. et al., 2014, PASP, 126, 359
Webbink R. F., 1984, ApJ, 277, 355
Wonnacott D., Kellett B. J., Stickland D. J., 1993, MNRAS, 262, 277
Wright E. L. et al., 2010, AJ, 140, 1868
Yi T. et al., 2022, Nat. Astron., 6, 1203
Zhang Z.-X., Liu H.-B., Yi T., Sun M., Gu W.-M., 2024, ApJ, 961, L48
Zheng L.-L. et al., 2022, ApJ, 936, 33
Zheng L.-L. et al., 2023, Sci. China Phys. Mech. Astron., 66, 129512
Zhou G. et al., 2020, ApJ, 892, L21

APPENDIX A: AN INJECTION-RECOVERY TEST

The PHOEBE models of J1208 and J1721 produce different predictions of the binary masses and inclinations depending on the *TESS* sector used and the number of spots. Here, we create a synthetic binary and attempt to recover the 'true' parameters using the same PHOEBE modelling process.

We generate a binary with a primary mass of $M_1 = 0.765\,\mathrm{M}_\odot$ and a secondary mass of $M_2 = 1.2\,\mathrm{M}_\odot$. We use a MIST evolutionary track with Solar abundances to select $T_{\rm eff} = 4760$ K and $R_1 = 0.69\,\mathrm{R}_\odot$ for the primary. The orbital inclination is set to $i = 72^\circ$ and the orbital period is $P = 0.34567$ d. We add a single spot to the primary star, with position $\theta_s = 47^\circ$, $\phi = 82^\circ$, size $R_s = 13^\circ$, and relative spot temperature $T_s/T_{\rm eff} = 0.80$.

We created a synthetic light curve using times matching the *TESS* observations from the J1721 and selected five random times for the RV observations. We then add random noise to each data set with uncertainties on the normalized flux of 1×10^{-4} and on the RVs of $0.1\ \mathrm{km\,s^{-1}}$. We follow the same PHOEBE modelling steps described in Section 4. Fig. A1 shows the posteriors as compared to the injected values. Although we find a secondary mass $M_2 = 1.17^{+0.04}_{-0.05}\ \mathrm{M}_\odot$ consistent with the true mass, the orbital inclination, and mass ratios are not recovered.

The spot positions also differ from the injected values. The PHOEBE model prefers a spot with a higher temperature ratio $T_s/T_{\rm eff} = 0.95$ and a slightly larger size $R_s = 21^\circ$. The spot position is also different with $\theta_s = 83^\circ$ and $\phi_s = 85^\circ$.

Although we only generated one synthetic binary, this test illustrates the challenges in recovering orbital parameters for spotted ELLs. The companion mass was recovered correctly in this case, but the inclination and spot parameters differ from the true values, suggesting that it is still risky to trust the results.

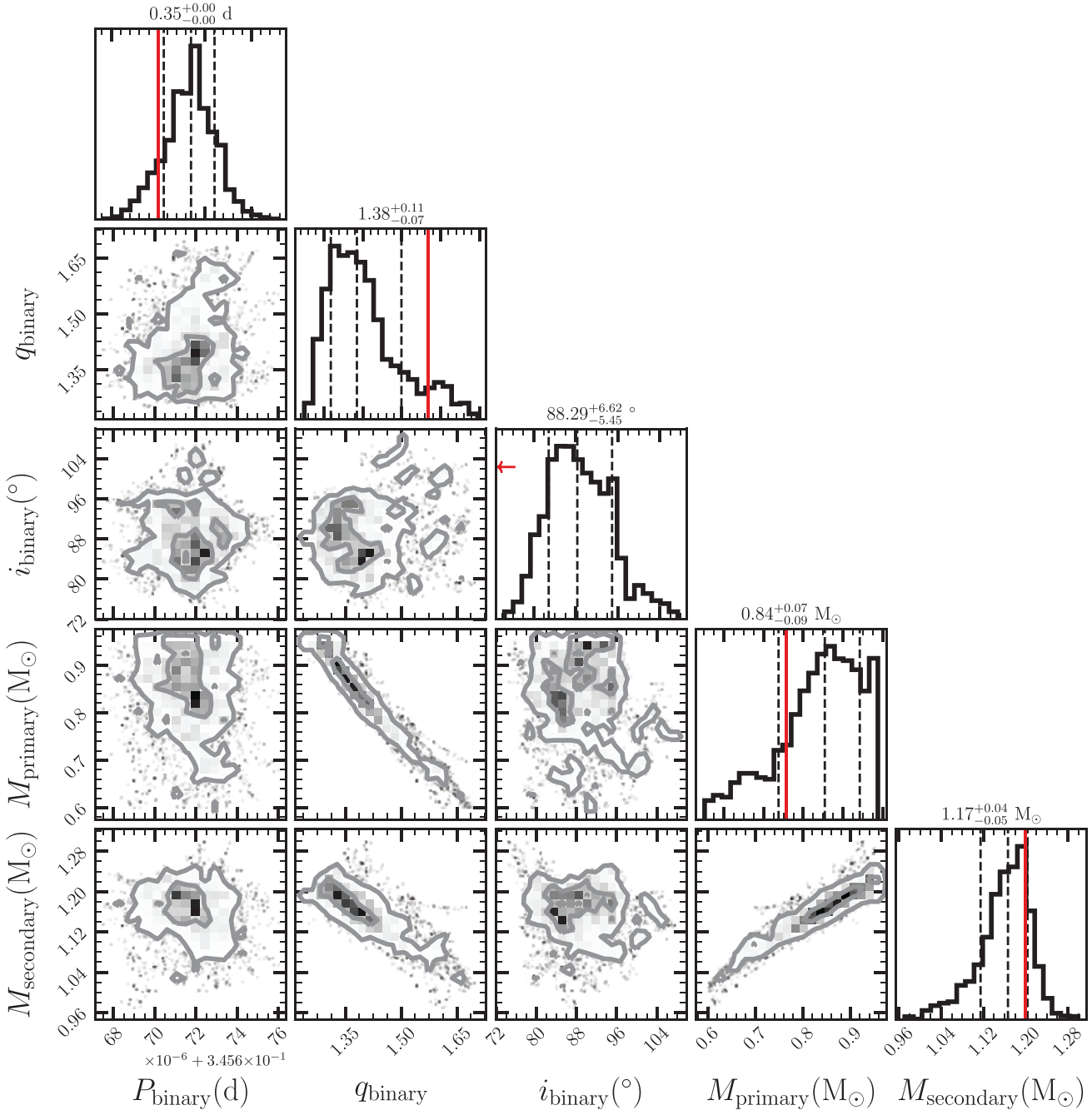

Figure A1. MCMC posteriors for the synthetic system. The red lines indicate the injected values. The synthetic binary inclination is outside the plot range, so an arrow is shown instead.

This paper has been typeset from a TEX/LATEX file prepared by the author.